Construction and Performance of Fine Grained Detector for T2K Experiment

Kyoto University Graduate School of Science
High energy physics group

Kei Ieki

January 28, 2010

Abstract

T2K (Tokai to Kamioka) is a long baseline neutrino oscillation experiment started in 2009. The properties of muon neutrinos produced at J-PARC (Japan Proton Accelerator Research Complex) are measured at both a near detector (ND280) and a far detector (Super Kamiokande), to measure the neutrino oscillation. The main goal of T2K is to measure the unknown mixing angle θ_{13} by observing conversion from the muon-type neutrino to the electron-type neutrino. To achieve high sensitivity for this measurement, it is important to measure the neutrino beam flux and energy spectrum for each flavor of the neutrino at the near detector, located at 280m from the neutrino production target.

The FGDs (Fine-Grained Detectors) are a main part of the near detector complex. They consist of layers of finely segmented scintillator bars and act as both neutrino interaction targets and tracking detectors. Photons from each scintillator bar are collected and transmitted to the end of the bar by a wavelength shifting fiber. Then the photons from each fiber are read out by the photon detector called MPPCs (Multi-Pixel Photon Counters).

The FGDs were assembled at TRIUMF (Canada) in 2008. After the assembly, we ran beam tests to test the readout electronics and to check the detector response to various types of beam particles. In 2009 summer we shipped the FGDs to Tokai, reassembled the detectors and tested with cosmic rays, then finally installed them to the ND280 pit in October 2009. We studied the performance of the FGDs and checked the calibration method during the beam test and cosmic tests, to be ready for neutrino beam data taking. The first neutrino beam run took place in December 2009, and we successfully observed the first neutrino candidate events.

Contents

1 **The T2K experiment** **8**
- 1.1 Neutrino and Neutrino oscillation 8
  - 1.1.1 Neutrino oscillation experiments 9
- 1.2 Overview of the T2K experiment 10
  - 1.2.1 J-PARC neutrino beam line 11
  - 1.2.2 Beam monitor 12
  - 1.2.3 Off-Axis method 12
  - 1.2.4 Near Detectors 14
  - 1.2.5 Far Detector (Super-Kamiokande) 16

2 **The Fine-Grained Detectors** **17**
- 2.1 The FGD and the ND280 Tracker 17
- 2.2 Requirements and design 18
  - 2.2.1 The requirements for the FGDs 18
  - 2.2.2 Overview of the design 19
- 2.3 Scintillators 21
- 2.4 Wavelength shifting fibers 21
- 2.5 Water modules 22
- 2.6 MPPC (Multi-Pixel Photon Counter) 23
- 2.7 Readout electronics 25
  - 2.7.1 Bus-boards and backplanes 25
  - 2.7.2 Front-end cards 26
  - 2.7.3 Waveform analysis 27

3 **Beam test at TRIUMF** **29**
- 3.1 Setup for the beam test 29
- 3.2 MPPC properties check 29
  - 3.2.1 Gain measurement 31
  - 3.2.2 Temperature dependence to gain 32
  - 3.2.3 Crosstalk + Afterpulsing 33
- 3.3 Hit pre-selection algorithm 34

4 Commissioning at J-PARC **41**
- 4.1 FGD reassembly work and installation into the pit 41
- 4.2 Commissioning and performance test 43
  - 4.2.1 Bad channels check 44
  - 4.2.2 Voltage scan and breakdown voltage measurement 47
  - 4.2.3 Cosmic trigger quality check 49
  - 4.2.4 Timing calibration 54
  - 4.2.5 Photo-electron yield per path length 58
  - 4.2.6 Hit efficiency of scintillator layers 59
- 4.3 Summary of the commissioning and tests before the beam run 64

5 Beam commissioning **65**
- 5.1 Summary of the beam run 65
- 5.2 Detection of neutrino events 66

6 Summary **70**

List of Figures

1.1 The overview of T2K experiment. 10
1.2 J-PARC neutrino beam line. 11
1.3 Schematic view of Muon Monitor 12
1.4 Concept of off-axis method. 12
1.5 Neutrino energy in the function of the momentum of parent pion, for different off-axis angles. 13
1.6 The neutrino energy spectrum for different off-axis angles (top) and the oscillation probability in the function of neutrino energy (bottom). 13
1.7 The near detectors located at 280 m downstream from the neutrino production target. 14
1.8 Schematic view of ND280 detectors 15
1.9 Super Kamiokande detector. 16

2.1 Simulation of CCQE interaction. 18
2.2 FGD architecture. 20
2.3 Cross section view of the scintillator bar. 21
2.4 Absorption and emission spectrum for Kuraray Y11 wavelength shifting fiber 22
2.5 Cross section of water panel. 23
2.6 Conceptual schematic of negative pressure system. 23
2.7 The overview of read out electronics for the FGDs 25
2.8 Picture at the end of the scintillator bars. The fibers are connected to the MPPCs with the optical connectors. The bus-board contains 16 MPPCs, and the ribbon cables connect the bus-boards and the backplane. 26
2.9 The front-end cards in FGD1, mini-crate 6. The LPB was not installed at this time. 27
2.10 An example of a waveform. The black(red) line shows the waveform before(after) data compression. 28
2.11 Example of pulse fitting. The black line shows the waveform, and the red line shows the fitted line. 28

3.1 Setup for the beam test 30
3.2 TRIUMF M11 beam line 30

3.3 Pulse height distribution of dark noise hits . . . 32
3.4 Gain vs. channel ID . . . 32
3.5 Temperature dependence of gain at $V_{over} = 0.85$ V . . . 33
3.6 Gain[19.5°C]/Gain[21.5°C] vs. Channel ID . . . 33
3.7 Example of pulse height sum distribution for one channel. Red line shows a fit to the sum of two Gaussians. . . . 34
3.8 Crosstalk + Afterpulsing probability vs. channel ID for 960 channels 35
3.9 Crosstalk + Afterpulsing probability result measured in M11 test - Measured in the test in Kyoto . . . 35
3.10 Concept of time clustering cut. Most of the noise hits are cut by the noise threshold PE_{noise}. Signals which occurred within T_{width} will be selected in the cluster. If the sum of pulse height is less than PE_{sum}, those hits will not be included in the cluster even if they occurred within T_{width}. . . . 36
3.11 Beam timing distribution. . . . 36
3.12 Beam timing distribution for 4 crates. Red, green, blue and yellow lines correspond to crate 4, 10, 13 and 19 respectively. . . . 36
3.13 Event display of beam track. Size of the circle represents the pulse height, color represents the pulse timing. Three lines shows the region to regard the hit as a particle hit. . . . 37
3.14 Number of particle hits per event vs. noise threshold . . . 38
3.15 Number of noise hits per event vs. noise threshold . . . 38
3.16 Pulse height sum of two pulses for particle hits (red) and noise hits (black). . . . 38
3.17 Example of event display without any cut. . . . 39
3.18 Example of event display with 2.5 p.e. threshold cut. . . . 40
3.19 Example of event display with 2.5 p.e. threshold and timing cut. . . . 40
3.20 Example of event display with all three cuts. . . . 40

4.1 Testing the MPPCs crate by crate by using a portable rack. . . . 42
4.2 Tilting the FGD to the vertical. All assembly works were done by muscle power. . . . 42
4.3 Installing the FGD. The crane slowly lowered the FGD into the basket. 43
4.4 Pulse height distribution of dark noise pulses (Normal channel) . . . 45
4.5 Pulse height distribution of "Dead" channels . . . 45
4.6 Pulse height distribution of "Low gain" channels . . . 45
4.7 Pulse height distribution of "High gain" channels . . . 45

4.8 FGD1 from down stream side. We hanged 2×2 scintillators on the front/back side of the FGD when we tested the vertical bars, and placed at the top/bottom of the FGD when we tested the horizontal bars. 46
4.9 Pulse height distribution (Normal channel) 47
4.10 Pulse height distribution (Bad channel) 47
4.11 1p.e. pulse height vs. Bias voltage 48
4.12 Breakdown voltage vs. channel ID 48
4.13 Gain vs. channel ID with the bias voltage derived according to the spec sheet provided by Hamamatsu Photonics. The gain was affected by the temperature. 49
4.14 Gain vs. channel ID with the bias voltage derived from the voltage scan. 49
4.15 Diagram to define cosmic trigger condition. 51
4.16 Concept of cosmic-ray selection. The trigger is generated when there are hits in both FGD1 and FGD2, for X(vertical) and Y(horizontal) bars. 51
4.17 Examples of event display of cosmic-ray events. Points are fitted by the straight line using least square method. Radius of each circle corresponds to the pulse height of that signal, and the color corresponds to the timing. 52
4.18 Number of hits in FGD1 (top view) 53
4.19 Number of hits in FGD2 (top view) 53
4.20 Number of hits in FGD1 (side view) 53
4.21 Number of hits in FGD2 (side view) 53
4.22 Angular distribution of cosmic tracks. Red(Black) line corresponds to the distribution in X(Y) projection. 54
4.23 Overview of FGD readout electronics. 54
4.24 Timing marker system. CTM sends the signal to all the FEBs at the same timing via CAT6 cables. 56
4.25 RMS of signal timing per event 57
4.26 Mean timing of cosmic-ray hits for crates (Before correction) 57
4.27 Mean timing of cosmic-ray hits for crates (After correction) 57
4.28 Difference of mean timing in two FGDs vs. the track angle. 58
4.29 Deposited energy per plane vs. path length in the layer. 59
4.30 Example of shower event. 60

4.31 Example of secondary track. 60
4.32 Example of accidental noise hit. 61
4.33 Example of un-straight track 61
4.34 Difference of the slope value of the fitted line between two FGDs. The red line shows the fitted line with Gaussian. 61
4.35 Mean residual for 44 layers, before(black) and after(red) the correction. 62
4.36 Hit efficiency of the layers. 63
4.37 Hit efficiency in the function of the distance from the center of the scintillator bar. 63
4.38 The expected angular distribution of muons at the near detector. The shaded region in this distribution represents the angular distribution of muons from CCQE interaction [10]. 64

5.1 Typical event which contains only few hits in the cluster. 67
5.2 Mean photo-electron vs. number of hits in the cluster. 67
5.3 Typical event which contains >10 hits in the cluster. 67
5.4 Number of hits in the cluster in the beam data. 68
5.5 Timing histogram of beam triggered events. (1bin = 100 ns) 68
5.6 Timing histogram of periodically triggered events. (1bin=100 ns) . . 68
5.7 Example of neutrino candidate event. 69

List of Tables

1.1 Summary table of beam parameters 11
2.1 Specifications for the FGDs 20
3.1 Summary of clustering cut. 39
4.1 Tested items and purposes 44
5.1 Summary of December neutrino beam run 65

Chapter 1

The T2K experiment

1.1 Neutrino and Neutrino oscillation

Neutrinos are the elementary particles which have very tiny mass and electrically neutral. They were first postulated by Pauli in 1930 in order to explain the continuum energy spectrum of electrons from β decay.
In the standard model, the types of neutrinos are believed to be three: ν_e, ν_μ and ν_τ.
The neutrino oscillation is a phenomenon that one type of neutrino changes into a different type of neutrino. It was first proposed by Pontecorvo as a consequence of finite neutrino masses.
The flavour eigenstate of neutrino $|\nu_\alpha\rangle$ $(\alpha = e, \mu, \tau)$ can be expressed by the superposition of neutrino mass states $|\nu_i\rangle$ (i = 1,2,3):

$$|\nu_\alpha\rangle = \sum_i U_{\alpha i}|\nu_i\rangle, \tag{1.1}$$

where U is a unitary matrix referred as MNS (Maki-Nakagawa-Sakata) matrix [1]. The MNS matrix can be expressed with four independent parameters: three mixing angles $\theta_{12}, \theta_{23}, \theta_{31}$ and one CP phase δ.

$$U = \begin{pmatrix} 1 & 0 & 0 \\ 0 & c_{23} & s_{23} \\ 0 & -s_{23} & c_{23} \end{pmatrix} \begin{pmatrix} c_{13} & 0 & s_{13}e^{-i\delta} \\ 0 & 1 & 0 \\ -s_{13}e^{-i\delta} & 0 & c_{13} \end{pmatrix} \begin{pmatrix} c_{12} & s_{12} & 0 \\ -s_{12} & c_{12} & 0 \\ 0 & 0 & 1 \end{pmatrix}, \tag{1.2}$$

where $c_{ij} = \cos\theta_{ij}$ and $s_{ij} = \sin\theta_{ij}$. Then the neutrino state generated as ν_α at t=0, x=0 can be written as:

$$|\nu_\alpha(t)\rangle = \sum_i U_{\alpha i} e^{-iE_i t + p_i x}|\nu_i(0)\rangle, \tag{1.3}$$

where E_i and p_i are respectively the mass and momentum of ν_i. Because of the tininess of neutrino mass, we can make replacements as following:

$$t \approx L, \tag{1.4}$$

$$E_i = \sqrt{p_i^2 + m_i^2} \approx p_i + \frac{m_i^2}{2p_i}, \tag{1.5}$$

where m_i is the mass of ν_i. By this replacements, Eq. (1.3) can be written as:

$$|\nu_\alpha(L)\rangle = \sum_i U_{\alpha i} e^{-i(m_i^2/2p_i)L} |\nu_i(0)\rangle, \tag{1.6}$$

Therefore the probability $P(\nu_\alpha \to \nu_\beta)$ that the flavour β will be observed after ν_α travels the distance L is:

$$\begin{aligned} P(\nu_\alpha \to \nu_\beta) &= |\langle \nu_\beta | \nu_\alpha(L)\rangle|^2 \\ &= \delta_{\alpha\beta} - 4\sum_{i>j} \mathrm{Re}(U^*_{\alpha i} U_{\beta i} U_{\alpha j} U^*_{\beta j}) \sin^2 \frac{\Delta m^2_{ij} L}{4E} \\ &\quad -2\sum_{i>j} \mathrm{Im}(U^*_{\alpha i} U_{\beta i} U_{\alpha j} U^*_{\beta j}) \sin^2 \frac{\Delta m^2_{ij} L}{2E}, \end{aligned} \tag{1.7}$$

where $\Delta m_{ij} = m_i^2 - m_j^2$. From the past experiments results, it is known that Δm^2_{12} is much smaller than the other two: $\Delta m^2_{23} \simeq \Delta m^2_{31} \gg \Delta m^2_{12}$. Hence, if we focus on the energy region $E_\nu \simeq \Delta m^2_{23} \cdot L$, the neutrino oscillation probability can be approximately calculated as following:

$$\begin{aligned} P(\nu_\mu \to \nu_e) &\simeq \sin^2 2\theta_{13} \cdot \sin^2 \theta_{23} \cdot \sin^2 \Delta_{23} \\ &\equiv \sin^2 2\theta_{\mu e} \cdot \sin^2 \Delta_{23}, \end{aligned} \tag{1.8}$$

$$\begin{aligned} P(\nu_\mu \to \nu_\mu) &\simeq 1 - \sin^2 2\theta_{23} \cdot \cos^4 \theta_{13} \cdot \sin^2 \Delta_{23} \\ &\equiv 1 - \sin^2 \theta_{\mu\tau} \cdot \sin^2 \Delta_{23}, \end{aligned} \tag{1.9}$$

$$P(\nu_e \to \nu_e) \simeq 1 - \sin^2 2\theta_{13} \cdot \sin^2 \Delta_{23}, \tag{1.10}$$

where $\Delta_{23} \equiv \Delta m^2_{23} L/4E, \sin^2 2\theta_{\mu e} \equiv \sin^2 2\theta_{13} \cdot \sin^2 \theta_{23}$, and $\sin^2 2\theta_{\mu\tau} \equiv \cos^4 \theta_{13}$. By measuring the probability of oscillations, we can measure the parameters θ_{13} and Δm^2_{13}.

1.1.1 Neutrino oscillation experiments

The parameters measured from recent neutrino oscillation experiments are summarized in the following.

θ_{23}, Δ^2_{23} (Atmospheric region)

The neutrino oscillation of the atmospheric neutrinos ($\nu_\mu \to \nu_x$) was discovered by Super-Kamiokande group[2]. This is the first discovery of the neutrino oscillation. The result was confirmed by K2K experiment[3] and MINOS[4] experiment using the ν_μ beam. The measured parameters were $\Delta m^2_{23} \sim 2.5 \times 10^{-3}$ eV^2 and $\theta_{23} \sim 45$ degrees.

$\theta_{12}, \Delta^2_{12}$ (Solar region)

The neutrino oscillation of the solar neutrinos ($\nu_e \rightarrow \nu_x$) was discovered by solar neutrino experiments (SNO[5], Super-Kamiokande[6]). The result was confirmed by reactor experiment (Kamland[7]). The measured parameters were $\Delta m^2_{12} \sim 8 \times 10^{-5}$ eV^2 and $\theta_{12} \sim 30$ degrees.

θ_{13}, δ

θ_{13} and δ have not been measured to be nonzero. According to the CHOOZ experiment [8](reactor neutrino, $\nu_e \rightarrow \nu_x$), the upper limit for θ_{13} is

$$\sin^2 2\theta_{13} < 0.15 \ (90\% \text{ C.L.}),$$

when $\Delta m^2_{23} \sim 2.4 \times 10^{-3}$ eV^2.

Since δ appears with $\sin\theta_{13}$ in the MNS matrix, it does not make any effect if $\theta_{13} = 0$. Therefore it is important to observe the non-zero value of θ_{13}.

1.2 Overview of the T2K experiment

The T2K experiment is the accelerator based long baseline neutrino oscillation experiment started in April 2009. The intense ν_μ beam are produced by J-PARC (Japan Accelerator Research Complex) proton accelerator at Tokai. We detect the neutrinos at both the near detector “ND280” and the far detector “Super-Kamiokande” (Fig. 1.1). Neutrino oscillation probability is measured by comparing the neutrino interaction rate at near/far detectors. The main goals of T2K experiment are:

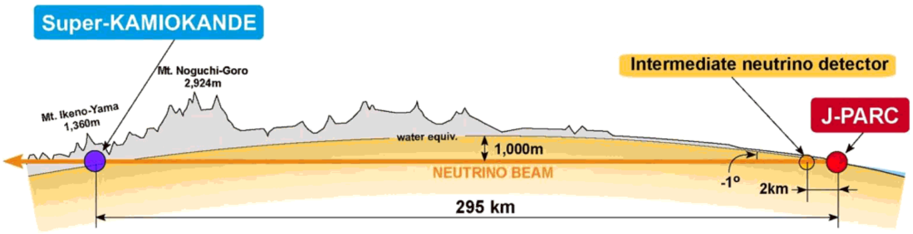

Figure 1.1: The overview of T2K experiment.

Discovery of $\nu_\mu \rightarrow \nu_e$ oscillation

We search for the undiscovered oscillation mode $\nu_\mu \rightarrow \nu_e$ to measure the θ_{13}. The goal is to extend the search down to $\sin^2 2\theta_{13} \sim 0.006$.

Precise measurement of oscillation parameters in $\nu_\mu \rightarrow \nu_x$ oscillation

We measure the parameter in θ_{13} and m^2_{13} with an accuracy of 1% and 3% respectively.

1.2.1 J-PARC neutrino beam line

The layout of J-PARC neutrino beam line is shown in Fig. 1.2. The protons are accelerated through linear accelerator (LINAC), 3 GeV proton-synchrotron (RCS), and main ring (MR). They are slow-extracted from the MR and transported to the neutrino production target. The protons smashes the carbon target located at the Target Station(TS). Secondary pions are produced by hadronic interactions of the protons with the target. The directions of pions are focused by three electro-magnetic horns. The target sits inside the first horn to collect and focus as many pions as possible. Then the pions decay to neutrinos in the 94 m of decay region ($\pi \rightarrow \mu\nu_\mu$). At the end of the decay volume, the remaining protons and pions are absorbed by the beam dump. Only the neutrinos and high energy muons will penetrate the beam dump.

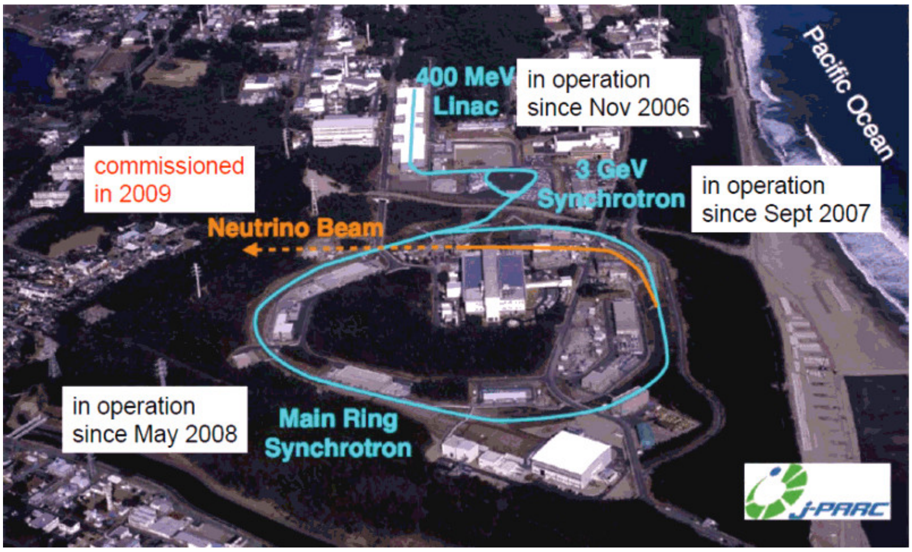

Figure 1.2: J-PARC neutrino beam line.

Designed parameters for the T2K beam are shown in the Table (1.1)

Beam energy	30 GeV
Beam power	0.75MW
Spill interval	~2.1 sec
Protons per spill	3.3×10^{14}p/spill
Bunches per spill	8/spill
Bunch interval	598 ns
Bunch width	58 nsec

Table 1.1: Summary table of beam parameters

1.2.2 Beam monitor

The muons which penetrates the beam dump are measured by the muon monitor (MUMON), which locates at just behind the beam dump. The MUMON monitors the intensity, profile and direction of the neutrino beam with the combination of ionization chambers array and silicon PIN photo-diodes array (Fig. 1.3).

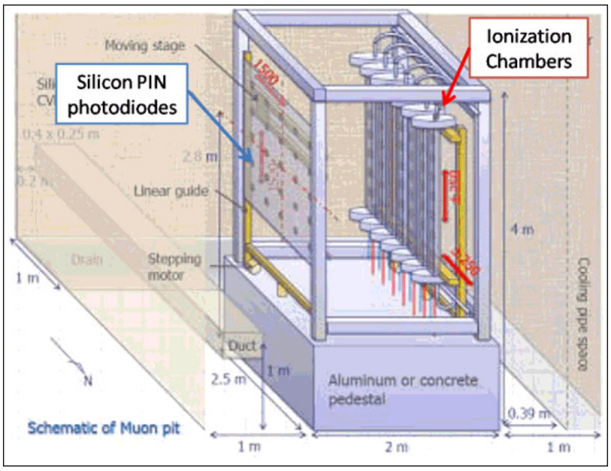

Figure 1.3: Schematic view of Muon Monitor

1.2.3 Off-Axis method

One of the important features of T2K is the off-axis beam. The concept of off-axis beam is shown in Fig. 1.4. The direction of neutrino beam is shifted ∼2.5 degree from the direction of far detector (Super-K).

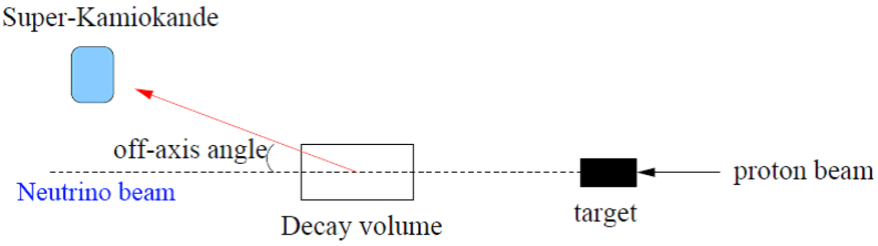

Figure 1.4: Concept of off-axis method.

When the neutrino produced from the pion decay $\pi \to \mu\nu$ in the direction of off-axis angle θ_{OA} with respect to the initial pion direction, the energy of the neutrino can be derived from following equation:

$$E_\nu = \frac{m_\pi^2 - m_\mu^2}{2(E_\pi - P_\pi \cos\theta_{OA})}. \tag{1.11}$$

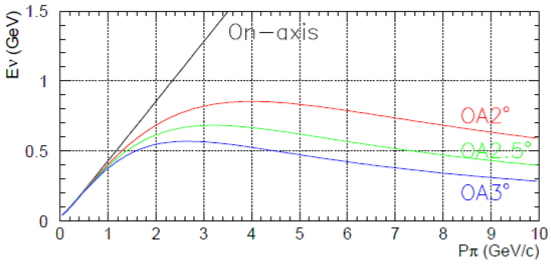

Figure 1.5: Neutrino energy in the function of the momentum of parent pion, for different off-axis angles.

With a finite off axis angle, the neutrino energy becomes almost independent of parent pion momentum (Fig. 1.5). Figure 1.6 shows the simulated neutrino energy spectrum with different off-axis angles and the oscillation probability as the function of neutrino energy. By using the off-axis method and adjusting the off-axis angle, we can make the narrow neutrino energy spectrum with a peak at where the oscillation probability becomes maximum. In addition, we reduce the backgrounds from high energy neutrinos by using the narrow energy spectrum beam. In T2K we set the off-axis angle to 2.5 degree.

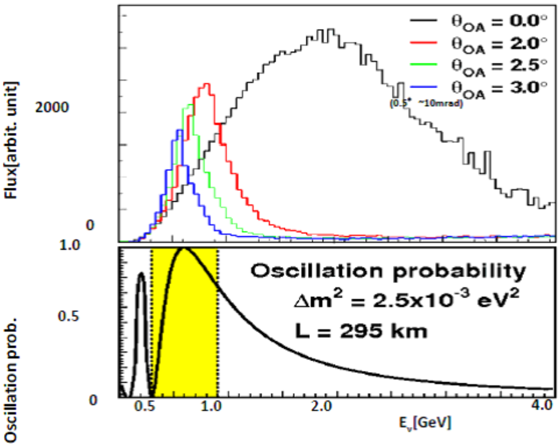

Figure 1.6: The neutrino energy spectrum for different off-axis angles (top) and the oscillation probability in the function of neutrino energy (bottom).

1.2.4 Near Detectors

The initial beam properties are measured by the near detectors, located at 280 m downstream from neutrino production target, $\sim$ 30 m underground in the pit. The near detector consists of the on-axis detector INGRID and the off-axis detector ND280 (Fig. 1.7).

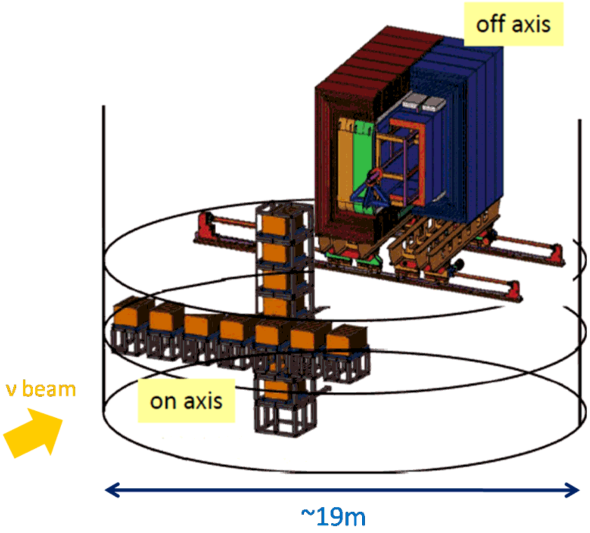

Figure 1.7: The near detectors located at 280 m downstream from the neutrino production target.

INGRID

The INGRID (Interactive Neutrino GRID) is located at the on-axis direction of the neutrino beam. It is designed to measure the beam direction by measuring the number of neutrino interactions in the modules. The INGRID consists of the identical modules aligned in the shape of a cross. Each module is made of plastic scintillators and irons.

ND280

The ND280 (Near Detector 280) is located at the off-axis direction (Fig. 1.8). It is designed to measure the initial neutrino beam flux, energy spectrum and also the background interaction rate. The ND280 consists of various types of detectors in the magnet:

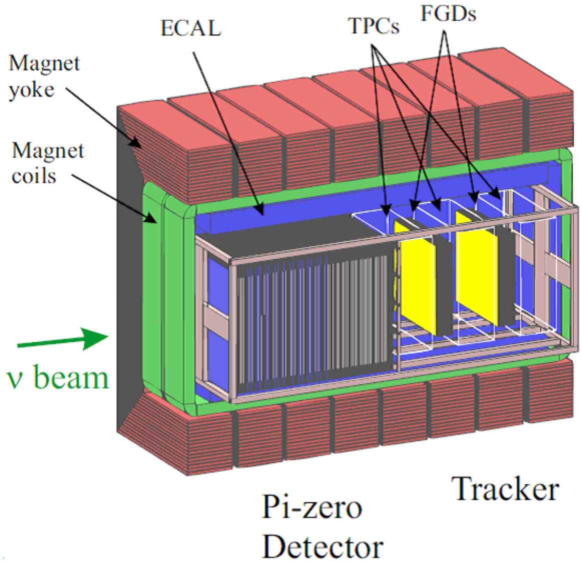

Figure 1.8: Schematic view of ND280 detectors

- Magnet
  ND280 uses the magnet which was used in UA1 experiment at CERN. It supplies a magnet field of 0.2 T to measure the momenta of charged particles produced by neutrino interactions. The inner size of the magnet is 3.5 m × 3.6 m × 7.0 m.

- Tracker
  Tracker consists of two FGDs (Fine-Grained Detectors) and three TPCs (Time Projection Chambers). It is optimized to measure the tracks of the charged particles from neutrino interaction. We report these detectors in detail from the next chapter.

- P0D (Pi-zero detector)
  P0D locates at the upstream side of the inner magnet. It is optimized to measure the π^0 generated by neutral current interaction. The P0D consists of plastic scintillators and water targets.

- ECAL (Electro-magnetic CALolimeter)
  ECAL surrounds the Tracker and P0D. The ECAL consists of the plastic scintillator layers interleaved with Pb foils. Its main purpose is to measure the γ-rays from π_0 decays which did not convert in the inner detectors. It also aim to detect the electrons generated from Charged Current interaction of ν_e.

- SMRD (Side Muon Range Detector)
  The scintillator pads are inserted in the gaps of magnet iron yokes. The SMRD

measures the range of muons from neutrino interactions that go in the side ways and missed the TPCs.

1.2.5 Far Detector (Super-Kamiokande)

The far detector Super-Kamiokande is 50 kt water Cherenkov detector which is located at 1000 m underground of Kamioka mine in Gifu (Fig. 1.9). The detector contains 11200 of 20 inch photo-multiplier tubes to detect the Cherenkov light from the charged particles from neutrino interactions.

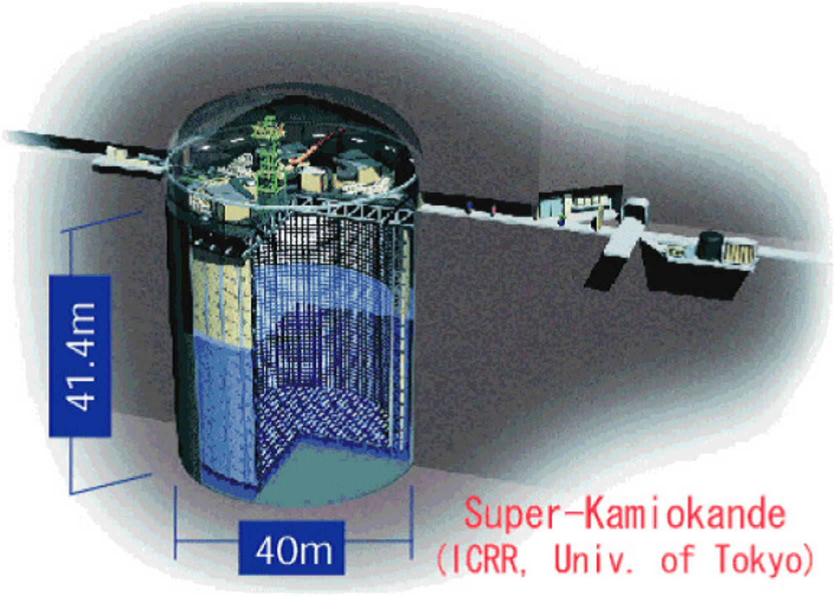

Figure 1.9: Super Kamiokande detector.

Chapter 2

The Fine-Grained Detectors

The FGD (Fine-Grained Detector) is a part of ND280 tracker system, and the finely segmented scintillator detector. In this chapter we report the requirements for the FGD and the actual design.

2.1 The FGD and the ND280 Tracker

The ND280 Tracker is composed of three TPCs (Time Projection Chambers) alternating with two FGDs. The Tracker is designed to detect the particle tracks from neutrino interaction in order to measure the neutrino beam flux, energy spectrum and flavour. The main signal for these measurement is the Charged-Current Quasi-Elastic interaction (CCQE) $\nu_l + p \to l + n$, which is the most common interaction at T2K's beam energy. Because these are 2-body interactions, the energy of the initial neutrino is reconstructed from the energy and direction of final leptons.

$$E_\nu = \frac{m_l^2 - 2m_p E_l}{2(E_l - m_p - p_l \cos\theta)}, \tag{2.1}$$

where θ is the angle of lepton momentum with respect to the beam direction. However, there exists many other background processes. For example, the CC-1π ($\nu_l + p \to l + n + \pi$) process has an additional pion in the final state, and thus it is not easy to reconstruct the initial neutrino energy for this interaction. In Super-K, because in most cases only the lepton in the final state has the momentum above the Cherenkov threshold in water, it is hard to distinguish the CC-1π background events from CCQE events. Therefore we need to measure the background event rates as well as CCQE interaction rate in the near detector.

To distinguish the types of neutrino interactions, it is important to detect the short tracks around the neutrino interaction vertex. In the ND280 Tracker, the FGD acts as both neutrino interaction target and the tracking detector. Therefore the short tracks such as a recoil proton should be measured in the FGD. Long tracks such as muons will reach the TPCs where their momenta and charges will be measured in the magnetic field (Fig. 2.1).

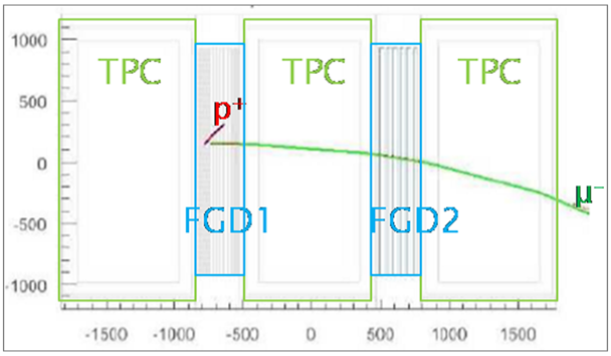

Figure 2.1: Simulation of CCQE interaction.

2.2 Requirements and design

2.2.1 The requirements for the FGDs

The requirements for the FGDs are listed below.

- They must be capable of detecting all the charged particles from the neutrino interaction vertex with a good efficiency. The direction and energy of those particles have to be measured to identify the type of neutrino interaction.

- They should be thin enough so that leptons in the final state enter the TPCs. The TPCs measure the momentum and charge of those particles.

- They must contain ~ 1 ton of target mass to provide enough statistics of neutrino events.

- They have to reliably distinguish the protons from muons and pions by measuring dE/dx.

- Since the FGD sits in an off-axis beam, the neutrino energy spectrum varies with the position across the detector. If the detector response is not uniform, the measurement of neutrino beam property will be complicated. Therefore the detector response has to be uniform across the detector.

- In order to compare the interaction rate with Super-K, it have to be capable of measuring the neutrino interaction rate in water. We will manage it by measuring the interaction rate of both carbon-based scintillator and a mixture of scintillator and water panel. We can then derive the interaction rate in water by statistically subtracting the rate of one from the other. For this reason the amount of high-Z materials in the detector must be minimized to compare the rate in water and carbon easily.

- They must have high acceptance for delayed hits from electrons from muon decay to identify the muon.

The final design is derived from K2K Scibar detector. The Scibar detector is composed of finely segmented scintillator layers and demonstrated an ability to detect CCQE and CC-nonQE interactions in the K2K experiment. With a number of modifications from the Scibar detector, and using the combination of the FGDs and the TPCs, the detector performance of the Tracker is expected to exceed the Scibar detector's performance for most physics measurements.

2.2.2 Overview of the design

The FGDs are composed of planes of scintillator bars which are oriented in either the x and y direction, perpendicular to the beam direction (Fig. 2.2). Each plane consists of 192 bars and has dimensions of 184.3 cm×184.3 cm×0.96 cm. The X planes (vertical bars) and Y planes(horizontal bars) forms an "XY module". The first FGD contains 15 XY modules. The second FGD contains 7 XY modules alternating with 6 target water modules.

The scintillator bars are 184.3 cm long and 0.96 cm×0.96 cm in the cross-section. Each bar is coated with TiO_2 for light reflection and contains the wavelength shifting fiber in the hole. The MPPCs (Multi-Pixel Photon Counters) collect the light from the scintillator bars via wavelength shifting (WLS) fibers at the end of the bars. The FGDs contains 8448 channels in total.

The XY modules and the target water modules hang inside the light-tight box called "dark box", which is made by aluminum. The read out electronics are mounted on the four sides of the FGDs, outside the dark box. In this way the heat producing elements are separated from the MPPCs, which have temperature dependence. The cooling water lines run through the four sides of the FGDs to keep the temperature stable.

The specification of the FGD is summarized in the Table 2.1

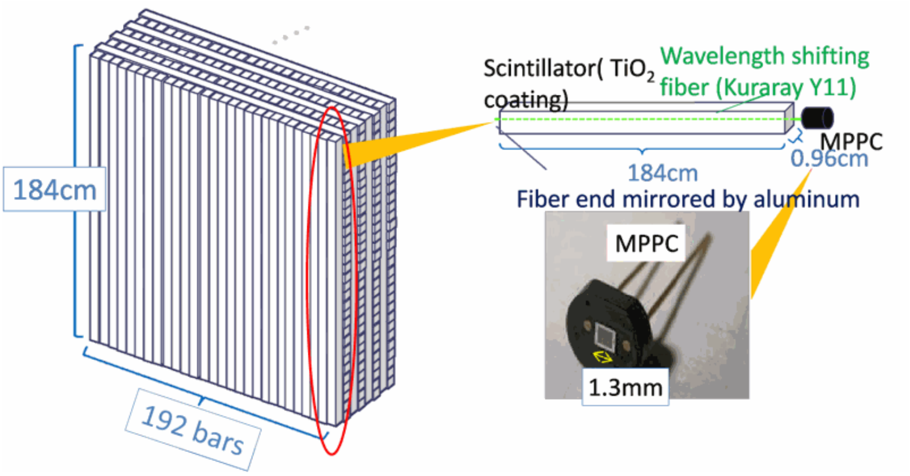

Figure 2.2: FGD architecture.

Structure	
Dimensions	184 cm×184 cm×33.6 cm for each FGD
Weight (FGD1)	1 ton
(FGD2)	0.56 ton(Scintillator) + 0.44 ton(Water modules)
Number of channels	5760(FGD1), 2688(FGD2)
Scintillator	
Material	Polystyrene, PPO(1%),POPOP(0.03%)
Reflector material	TiO_2(15%) infused in polystyrene
Dimensions	0.96 cm × 0.96 cm × 184.3 cm
WLS fiber	
Type	Kuraray Y11(200) S-35
Absorption peak wavelength	430 nm
Emission peak wavelength	476 nm
Diameter	1mm
Length	$\sim$ 2 m
Attenuation length	350 cm
Reflective coating	Coated by aluminum sputtering
MPPC	
Active area	1.3 mm × 1.3 mm
Pixel size	$50 \times 50\ \mu m^2$
Number of pixels	667

Table 2.1: Specifications for the FGDs

The details of each component are described in the following sections.

2.3 Scintillators

The scintillator bars are made of polystyrene doped with PPO and POPOP, and are co-extruded with a reflective coating consisting of polystyrene doped with 15% TiO_2. They were produced at Celco Plastics Ltd in Surrey, B.C. The geometrical specification as follows:

- Length (z dimension) = 1845.1±1 mm
- Outside x and y dimensions = 9.6±0.2 mm
- TiO_2 thickness = 0.25±0.05 mm (co-extruded bar coating)
- Active dimensions = 9.1±0.2 mm
- Hole diameter = 1.8±0.3 mm

The cross section view is shown in Fig. 2.3. The bars were glued together with 0.25mm G10 sheets to add mechanical rigidity and allow for easier handling. For the glue we used Plexus MA590.

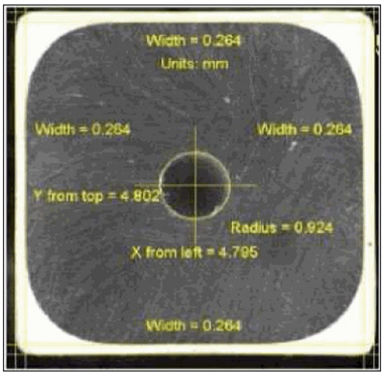

Figure 2.3: Cross section view of the scintillator bar.

2.4 Wavelength shifting fibers

Light from each scintillator bar is collected and transmitted by a blue-to-green double-clad wavelength shifting fiber. The Kuraray Y11 (200) S-35 type was selected to use for the FGDs. The specification of this fiber as follows:

- Diameter: 1.2 mm
- Fiber length: ~2 m
- Refractive index: 1.59(outer clad)/1.49(middle clad)/1.42(core)

- Absorption wavelength: 430 nm (peak)
- Emission wavelength: 476 nm (peak)
- Attenuation length: ~350 cm
- Decay time: ~7 ns
- Trapping efficiency by total internal reflection: ~5%

The absorption and emission spectrum of this fiber is shown in Fig. 2.4. The fibers were mirrored by aluminum sputtering and protected with UV epoxy at FNAL Lab 7.

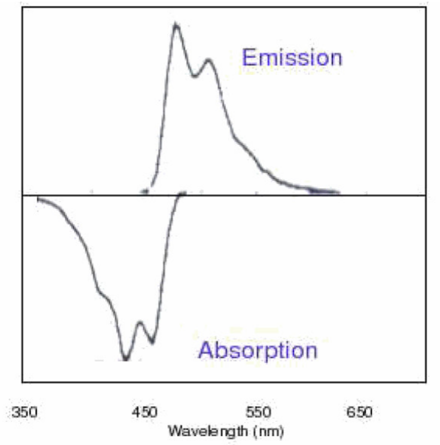

Figure 2.4: Absorption and emission spectrum for Kuraray Y11 wavelength shifting fiber

2.5 Water modules

The second FGD contains 6 water modules to measure the cross-section of neutrino interaction on a water target. The vessel is made of 25 mm thick polycarbonate (Lexan©) hollow panel, which is commercially made for fabrication of greenhouses. The interior of the panel is divided into 12.5 mm × 25.4 mm rectangular shells, which is further subdivided by a thin curved wall (Fig. 2.5). This structure provides enough strength to the water modules with the minimum amount of plastic.

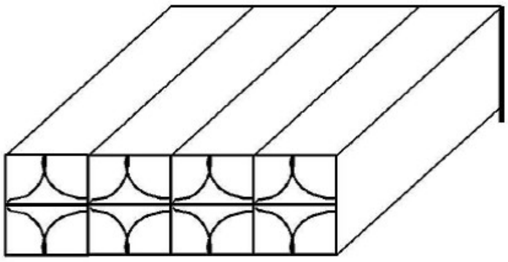

Figure 2.5: Cross section of water panel.

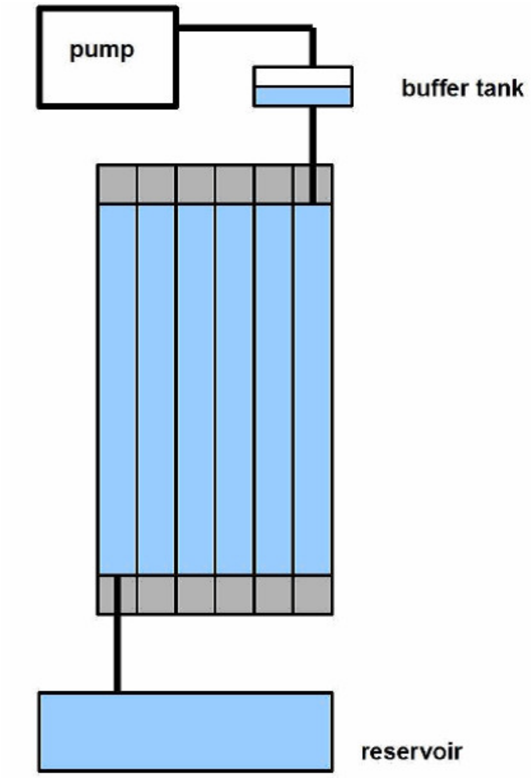

Figure 2.6: Conceptual schematic of negative pressure system.

We design that the water never leaks, to avoid a damage to the detector. For this purpose, we implement a negative pressure system (Fig. 2.6). The pump at the top sucks with just enough pressure to pull the water level in the polycarbonate vessel to the desired height. In this way the pressure of water is always kept below atmospheric pressure, hence the water never leaks even if there is any pinholes or hairline cracks.

2.6 MPPC (Multi-Pixel Photon Counter)

The light from the scintillator bars are detected by the MPPCs via wavelength shifting fibers at the end of the bars. The MPPC is a photon counting device manufactured by Hamamatsu photonics. It consists of many small avalanche photo-diodes (APDs) in an area of typically 1mm^2. Each APD pixel outputs a pulse signal when it detects one photon. The sum of the output of each APD pixels forms the MPPC output. The MPPCs are used in all of the ND280 detectors except for the TPCs. It satisfies the following requirements:

- Counting photons down to one photo-electron level.

- Works inside the 0.2 T magnetic field.
- Compact enough to fit in a very tight space constraint.

They also have following disadvantages:

- Temperature dependence
- High dark noise rate (few hundred kHz)

We use the special type of MPPC, with a sensitive area of 1.3×1.3 mm^2 containing 667 pixels with 50×50 $\mu\mathrm{m}^2$ size each, which was developed for the T2K experiment. The FGDs use 8448 channels of MPPCs. All of them were produced by Hamamatsu Photonics and their basic features were measured by the Kyoto group[9]. There are several parameters which characterize the MPPCs:

Breakdown voltage

When the bias voltage for the MPPC is higher than the specific voltage called the "breakdown voltage" V_{bd}, the output charge of the MPPC linearly increases as follows:

$$\text{Output charge} = \mathrm{C}(V_{bias} - V_{bd}),$$

where C is the capacitance of each APD pixel and V_{bias} is the bias voltage. The voltage above the breakdown voltage is called as "overvoltage" V_{over}. The typical breakdown voltage is ∼70 V. The V_{bd} depends on the temperature.

Gain

The gain represents the ratio of outputted charge to the input photo-electrons. In the test in Kyoto, we defined this parameter as the output charge for 1p.e. The typical value was $\sim 10^5$, and the gain linearly increases as the overvoltage increases.

Dark noise rate

The MPPC generates dark noise signals even if there are no input photoelectrons. The rate of dark noise is typically several hundred kHz. It depends on the over voltage and temperature.

Crosstalk + Afterpulsing probability

Crosstalk and Afterpulsing are the phenomena which make the output signal bigger than originally it was.

Crosstalk$\cdots$Photon from an avalanche generates another avalanche in a neighbor pixel.

Afterpulsing$\cdots$Electron from an avalanche is trapped in the lattice defect, re-emitted later, and makes a second avalanche in the same pixel.

They increases as the over voltage increase.

PDE(Photon Detection Efficiency)

> PDE is the efficiency to detect the photons. In the test in Kyoto, this parameter was measured relative to the PMT (Hamamatsu R1818). Typically the PDE is ∼ 1.5 times larger than the PMT.

In the test in Kyoto, we measured these parameters with different bias voltages (0.1V step) and in different temperatures (15°C, 20°C and 25 °C). All of the measured parameters fulfilled the requirements for the ND280 detectors.

2.7 Readout electronics

The hit signals from the MPPCs are recorded by special boards which were developed for the FGDs. In this section we describe the readout system of the FGDs.
The overview of the readout electronics is summarized in Fig. 2.7. The MPPCs are controlled and read out by the front-end cards which are installed in the "Mini-crates" on the four sides of the FGDs. There are six mini-crates on each side of the FGD. The mini-crates read out the waveform of MPPCs via "bus-boards" and "backplanes", and send the data to the back-end electronics modules, which are located outside the magnet.

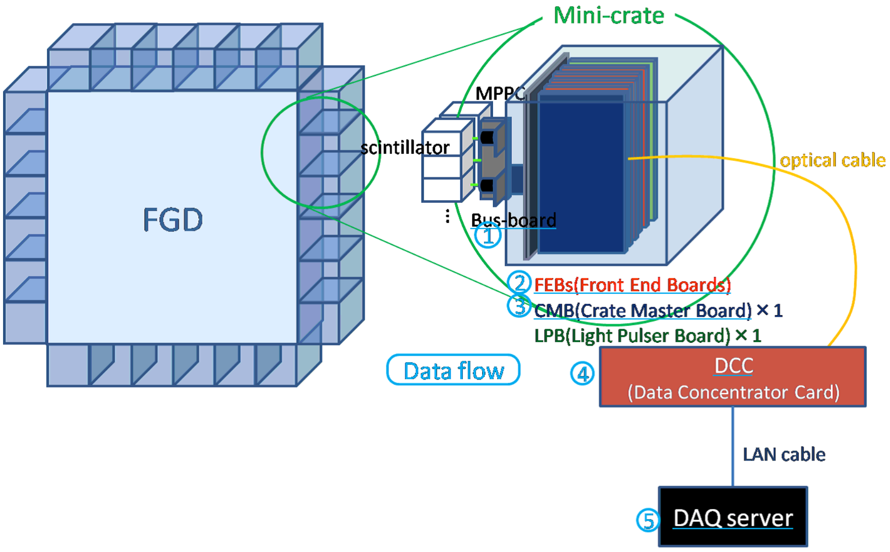

Figure 2.7: The overview of read out electronics for the FGDs

2.7.1 Bus-boards and backplanes

The MPPCs are mounted on the bus-boards. Each bus-board carries 16 MPPCs. On the bus-boards, the MPPCs are connected to the wavelength shifting fibers via

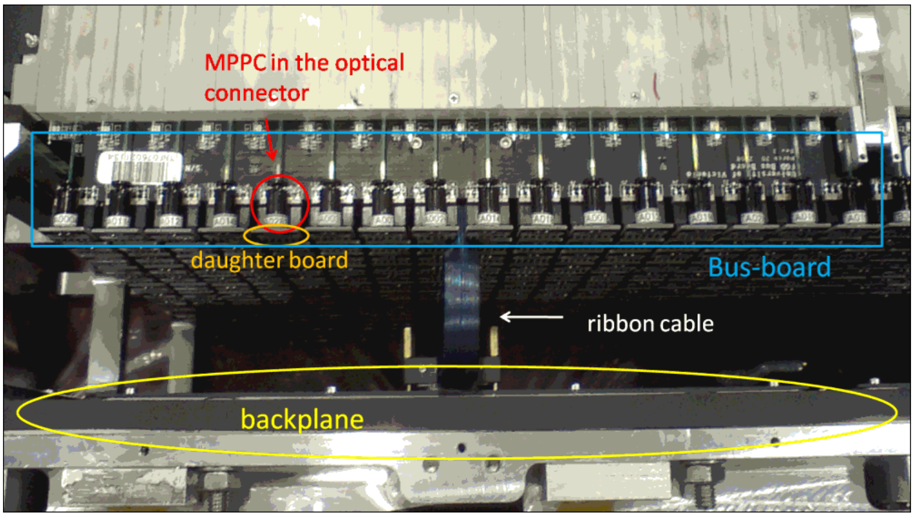

Figure 2.8: Picture at the end of the scintillator bars. The fibers are connected to the MPPCs with the optical connectors. The bus-board contains 16 MPPCs, and the ribbon cables connect the bus-boards and the backplane.

the optical connector (Fig. 2.8). The MPPCs are connected to the bus-board via the daughter boards. The signal from the MPPCs are then transmitted to the backplanes by ribbon cables. The backplanes connect the ribbon cables to the mini-crates which are located outside the dark box. The bus-boards also contain 16 LEDs and 2 temperature sensors for MPPC calibration.

2.7.2 Front-end cards

The front-end cards read out the waveforms of MPPCs in the mini-crate. Each mini-crate handles 15(7) Modules × 16 channels/bus-board = 240(112) MPPC channels for FGD1(FGD2). The following boards are installed in the mini-crates:

FEB(Front-End Board)

This board sets the bias voltage for the MPPCs and reads out the waveform. The SCA(Switched Capacitor Array) continuously records the waveform at 50MHz, for 10μs. One FEB handles 64 MPPC channels. For each mini-crate, there are 4(2) FEBs installed for FGD1(FGD2).

CMB(Crate Master Board)

This board contains the FPGA (Field Programmable Gate Array) to control the FEBs on the same mini-crate. The CMB reads out the data from the FEBs, compresses the data, and transmits them to the back-end electronics module called the DCC(Data Concentrator Card).

LPB(Light Pulser Board)

This board controls the LEDs on the bus-boards. Each mini-crate contains one LPB.

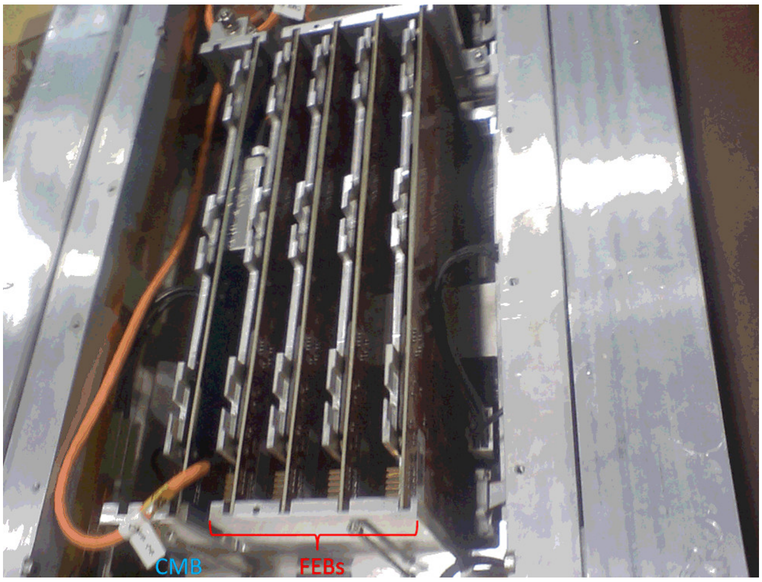

Figure 2.9: The front-end cards in FGD1, mini-crate 6. The LPB was not installed at this time.

2.7.3 Waveform analysis

The CMBs run the pulse finder to find a hit signal. They can reduce the data size by recording the waveform only around the pulse (Fig. 2.10). Furthermore, it can reduce the data size by only recording the pulse height and pulse timing of each pulse, or by discarding all the pulses whose pulse height is below the threshold.
The SCA on the FEBs performs waveform digitization at 50MHz, which corresponds to 20 ns of integration time window. To retrieve the timing resolution, we stretch the pulse with a pulse shaper and fit the pulse (Fig. 2.11). The fitting function is derived from the convolution of the MPPC response with the pulse shaper response:

$$x = (t - p_2)/p_3, \tag{2.2}$$

$$f(x) = \begin{cases} p_0 + p_1 \times x^4 \times (1 - x/p_4) \times e^{-x} & (x \geq 0), \\ p_0 & (x < 0), \end{cases} \tag{2.3}$$

where $p_0 - p_4$ are the fitting parameters and t is time. In this function, p_0 corresponds to the baseline of the waveform and p_2 corresponds to the pulse start timing.

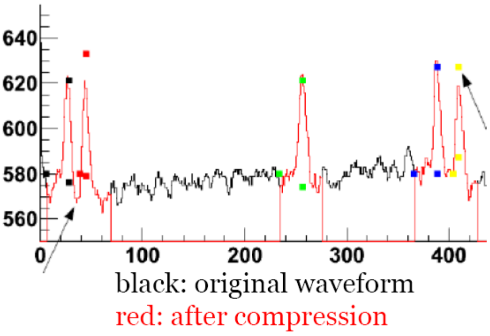

Figure 2.10: An example of a waveform. The black(red) line shows the waveform before(after) data compression.

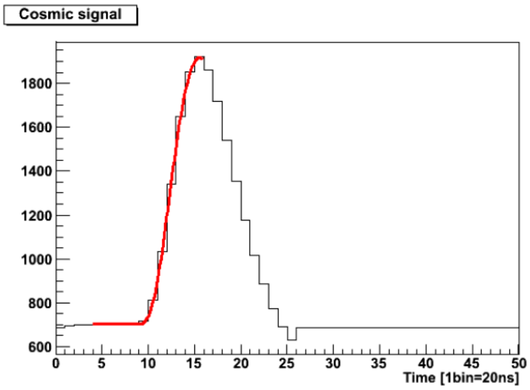

Figure 2.11: Example of pulse fitting. The black line shows the waveform, and the red line shows the fitted line.

Chapter 3

Beam test at TRIUMF

The FGDs were assembled at TRIUMF(Canada) in June∼December 2008. After the assembly, we performed a beam test from August 2008 to May 2009 in TRIUMF's M11 beam line to check the response of the detector to various types of beam particles together with the test of electronics.

In this chapter, we report the MPPC properties check and hit pre-selection method which were both necessary for cosmic-ray/beam data taking.

In the first section we summarize the setup for the beam test. In the second section we describe the property of MPPCs on the detector. We measured the features of the MPPCs such as their gain, temperature effect and crosstalk + afterpulsing probability, which is necessary to understand the performance of MPPCs in the real detector. In the third section we report the development of an algorithm to cut the noise hits and to select the particle hits.

3.1 Setup for the beam test

Figure 3.1 and 3.2 shows the setup for this beam test. The M11 beam line provides beams of $e^{\pm}, \mu^{\pm}, \pi^{\pm}$, and p with a momentum range of 100∼400 MeV/c. In this beam test, the readout electronics were not fully installed for most of the time. For this analysis, we use the data taken in the period when only 4 out of the 24 mini-crates in FGD1 were populated. In total 960 channels were active in this data.

3.2 MPPC properties check

The FGDs contain 8448 MPPCs to read out the light from each scintillator bar (see section 2.6). The MPPCs were produced by Hamamatsu Photonics, and their basic features were measured by the Kyoto group before shipping to Canada[9]. In order to calibrate the MPPCs, we need to know how those features affect the data in the real detector. Therefore, as an initial step, we checked the effect of those features in the beam test data.

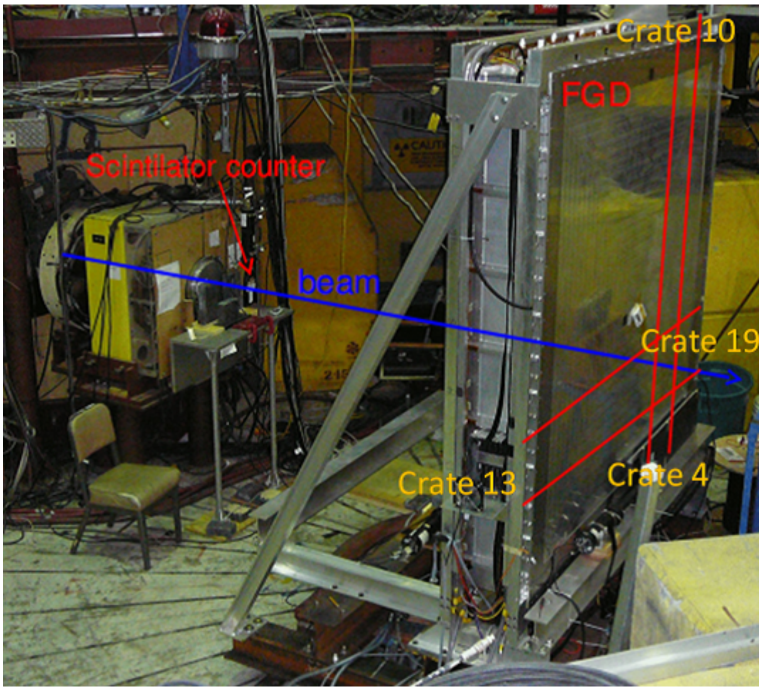

Figure 3.1: Setup for the beam test

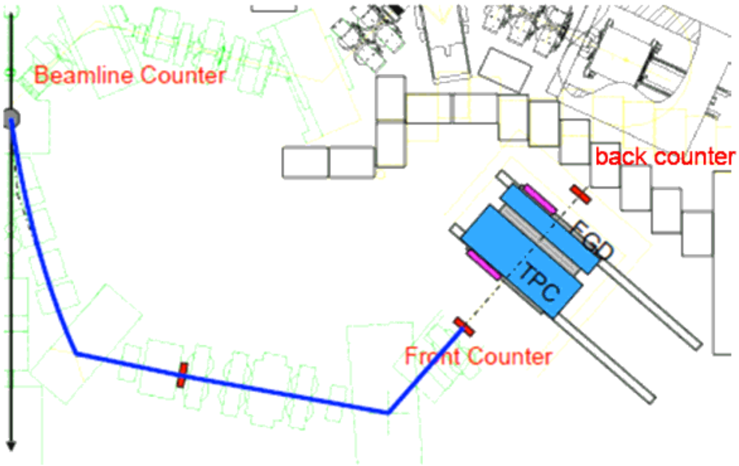

Figure 3.2: TRIUMF M11 beam line

We checked the following items:

Gain

This parameter determines the ratio of output signal to input photo-electrons. In the test at Kyoto, it was defined as the output charge of 1 p.e. hit. While for FGD, we define this parameter as the pulse height of 1 p.e. hit.

$$\text{Gain} \equiv 1 \text{ p.e. hit pulse height.}$$

We need to measure the gain during the data taking to convert the pulse height to an equivalent number of photo-electrons. We tested this procedure to measure the gain.

Temperature dependence

The gain of MPPCs varies with the temperature. For a constant bias voltage, the gain decreases as the temperature increases. Therefore, in order to keep the gain of MPPCs uniform, we need to adjust the bias voltage according to the temperature fluctuation. We measured the temperature dependence of gain by using the temperature sensors mounted on the bus-boards, and compared the result with the result from the test in Kyoto.

Crosstalk-Afterpulsing probability

Crosstalk and Afterpulsing are phenomena which will make the output signal from MPPCs bigger than the real signal. We need to take this effect into account in order to know the real signal size. We measured the probability of these phenomena to occur and compared it with the result from the test in Kyoto.

During these measurements, the voltage for all the MPPCs were set to $V_{over} = 0.85$ V, according to the spec sheet provided by Hamamatsu Photonics.

3.2.1 Gain measurement

First we measured the gain of the MPPCs. The gain is defined as the pulse height of 1 p.e. hit. The gain is most basic parameter for deriving the number of photo-electrons from the pulse height. If we neglect the second order effects such as crosstalk and afterpulsing, we can convert the pulse height(ph) of the hit signal to photo-electrons(pe) by the formula below.

$$pe = ph/gain. \tag{3.1}$$

The 1 p.e. pulse height can be derived from the pulse height distribution of the dark noise. Figure 3.3 shows an example of the pulse height distribution of dark noise. We derived the 1 p.e. pulse height by fitting the first peak in this distribution by a Gaussian.

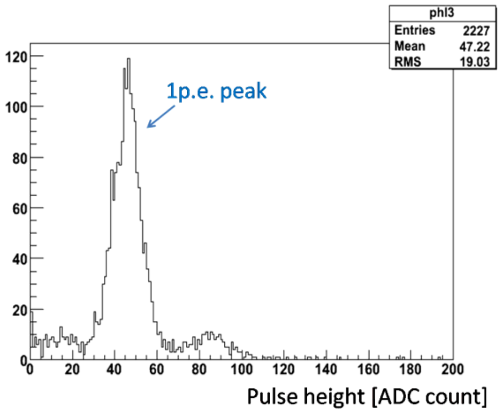

Figure 3.3: Pulse height distribution of dark noise hits

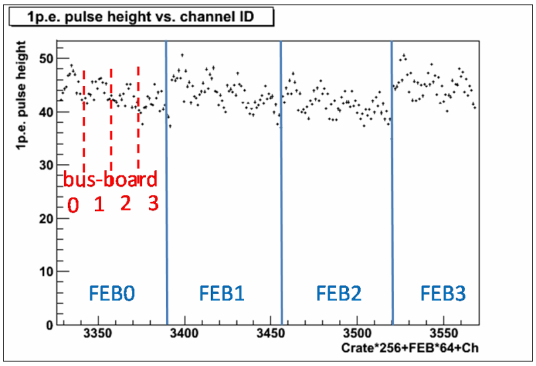

Figure 3.4: Gain vs. channel ID

In this way we measured the gain. Figure 3.4 shows the measured gain in mini-crate 13. The 1 p.e. pulse height looks basically the same for all the channels, but there was a weird pattern found for every 16 channels, which is considered as corresponding to different attenuations in each bus-board channel due to differences in trace path length on the board.

We need to correct this effect. Additional analysis is ongoing to understand this pattern and to apply the correction. However, for the time being, we simply use the formula 3.1 to convert the pulse height to photo-electron.

3.2.2 Temperature dependence to gain

The breakdown voltage of the MPPCs is known to have temperature dependency. A 1°C temperature increase corresponds to ∼0.06 V breakdown voltage increase[9]. Therefore if the bias voltage is constant, the overvoltage decreases as the temperature increases, and thus the gain decreases as the temperature increases. We measured this temperature effect and compared the measured result with the result from the test in Kyoto.

In order to measure the temperature, we use the sensors mounted on the bus-boards. For this analysis, we defined the temperature of each bus-board as the mean temperature of two sensors on it.

First, we checked the gain in several runs taken with same bias voltage but at different temperatures. Since the water cooling system was not implemented for these runs, temperature around the MPPCs was affected by the room temperature and fluctuated around 19°C∼22°C. Figure 3.5 shows the gain of one channel for 6 different temperature points. As we expected, the gain decreased linearly as the temperature increased. One degree temperature increase corresponded to ∼2.3 ADC channels gain decrease.

To compare this result with the result from the test in Kyoto, we checked the ratio of gain at 19.5°C and 21.5°C and compared it with the value we expect from the test in Kyoto. Figure 3.6 shows the result. Red line in the figure shows the expected ratio from the test in Kyoto. Except for 5 bad channels, the measured ratio was consistent with the result from the test in Kyoto. The expected ratio was 0.878, while the measured ratio was 0.876 with RMS=0.047.

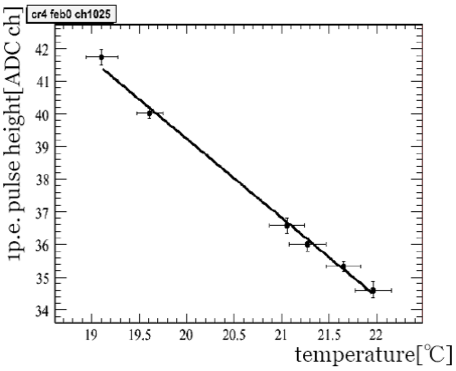

Figure 3.5: Temperature dependence of gain at $V_{over} = 0.85$ V

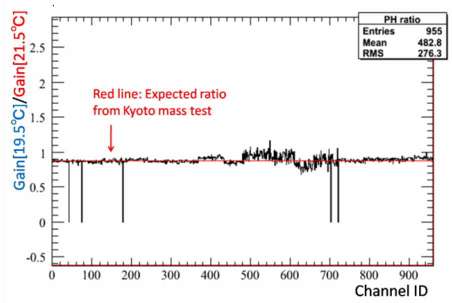

Figure 3.6: Gain[19.5°C]/Gain[21.5°C] vs. Channel ID

3.2.3 Crosstalk + Afterpulsing

As explained in section 2.6, both Crosstalk and Afterpulsing are the phenomena which will make the output hit signal bigger than the original hit signal. For example, Crosstalk + Afterpulsing probability is ~0.07 when $V_{over} = 0.8$ V[9], thus the 30 p.e. signal will be outputted as $30 \times 1.07 = 32.1$ p.e. We need to correct this effect to measure the true light yield. We measured the Crosstalk + Afterpulsing probability during the beam test and compared the measured probability with the probability measured at the test in Kyoto.

We calculated the Crosstalk + Afterpulsing probability by using basically the same method which was used at the test in Kyoto:

1. In the waveform, calculate the sum of pulse height of the pulses found in each 200 ns. The number of events for 0 p.e., 1 p.e. $\cdots$ in principle follows a Poisson distribution.

2. Make the distribution of the pulse height sum. Calculate the actual number of 0 p.e., 1 p.e. from the distribution in the following ways.
   0 p.e. $\cdots$ Count the number of events at pulse height sum = 0.
   1 p.e. $\cdots$ Fit the distribution by Gaussians, then integrate the fitted function of the first peak from mean-5σ to mean+5σ (Fig. 3.7)

3. Assuming the Poisson distribution, we can estimate the number of 1 p.e. events by the number of 0 p.e. events and the number of all events.

$$\begin{aligned} N_{0p.e.} &= N_{all} e^{-\lambda}, \\ N_{1p.e.}^{exp} &= N_{all} \lambda e^{-\lambda} \\ &= -N_{0p.e.} \ln(N_{0p.e.}/N_{all}), \end{aligned}$$

where N_{all}, $N_{0p.e.}$ and $N_{1p.e.}^{exp}$ represent number of all events, number of 0 p.e. events and number of expected 1 p.e. events respectively. However, the actual number of 1 p.e. events is usually observed less than expected, because of the Crosstalk + Afterpulsing effect. Therefore, we can calculate the Crosstalk + Afterpulsing probability by the formula below.

$$\text{Crosstalk + Afterpulsing probability} = 1 - \frac{\text{1p.e. events observed}}{\text{1p.e. events expected}}. \tag{3.2}$$

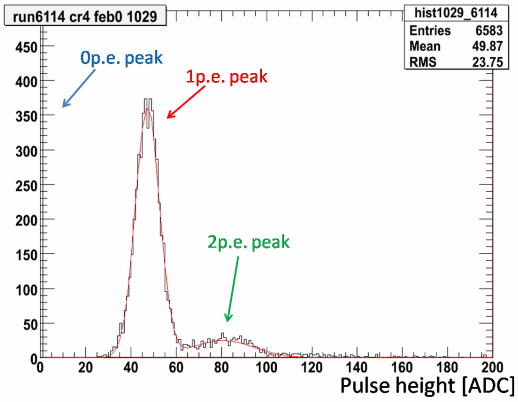

Figure 3.7: Example of pulse height sum distribution for one channel. Red line shows a fit to the sum of two Gaussians.

Figure 3.8 shows the result for 960 channels. The Crosstalk + Afterpulsing probability was distributed uniformly over all the channels, except for two spikes due to broken channels. Figure 3.9 shows the Crosstalk + Afterpulsing probability compared with the result from the test in Kyoto. The result was consistent with the result from the test in Kyoto. The mean Crosstalk + Afterpulsing probability was only 0.01 higher than expected, and the RMS of the difference was 0.01.

3.3 Hit pre-selection algorithm

The MPPCs have high noise rates (few hundred kHz), and the pulse height of those noise hits sometimes get higher than a few p.e. due to the effect of Crosstalk and

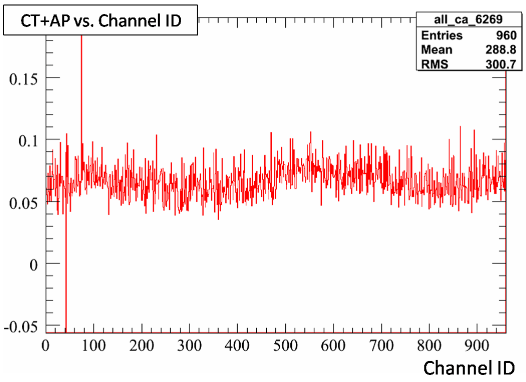

Figure 3.8: Crosstalk + Afterpulsing probability vs. channel ID for 960 channels

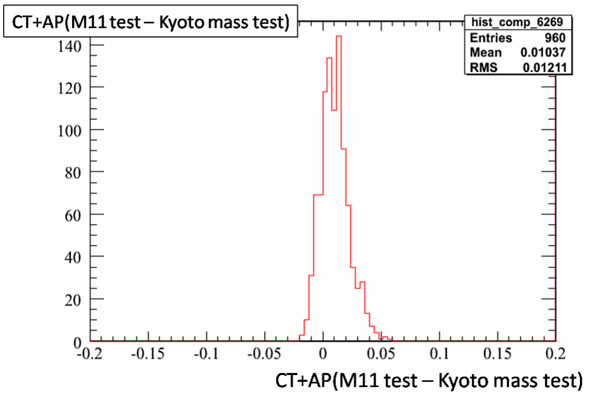

Figure 3.9: Crosstalk + Afterpulsing probability result measured in M11 test - Measured in the test in Kyoto

Afterpulsing. Therefore, to cut the noise hits, we need to create a hit selection algorithm based on the hit timing and pulse height of the hit.
We developed an algorithm called "Time clustering" for this pre-selection. We will use this cut as a low level hit selection before moving on to more high level analysis. The outline of this algorithm is follows (Fig 3.10).

1. Cut most of the noise hits by a cut at low p.e. threshold PE_{noise}.
2. Sort all the hits in time.
3. For each hit, check if the hit satisfies the clustering conditions below.
    - Has another hit within time T_{width}
    - Sum of the pulse height of the hit itself and the other hit is greater than the threshold PE_{sum}

We adjusted these three parameters PE_{noise}, T_{width} and PE_{sum} using the beam test data. For this analysis, we used 250 MeV/c muon beam runs, whose trigger condition was coincidence of scintillators hits located at the front/back sides of the FGD. Since muons always penetrate the FGD for this run, it is easy to reconstruct the particle track and to distinguish particle hits from noise hits. The voltage of the MPPCs was again set to $V_{over} = 0.85$ V.

1. Timing width T_{width}
First we determined the timing width. This parameter defines how close the readout timing of particle hits should be. To determine this parameter, we checked the distribution of beam timing (Fig. 3.11) by simply cutting the noise hits with a 10 p.e. threshold. From the width of the peak timing, we determined the timing width

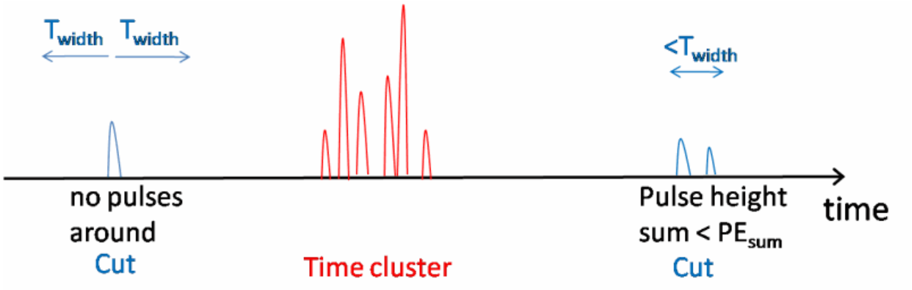

Figure 3.10: Concept of time clustering cut. Most of the noise hits are cut by the noise threshold PE_{noise}. Signals which occurred within T_{width} will be selected in the cluster. If the sum of pulse height is less than PE_{sum}, those hits will not be included in the cluster even if they occurred within T_{width}.

T_{width} as 80ns. The 80ns seems to be too long for the hit from one particle, but it includes the difference of time offset between the crates. Figure 3.12 shows the timing distributions for 4 different crates. Different color correspond to the timing distributions of different crates in this figure. Peak timing is clearly different due to the different time offsets for the crates. This timing width is smaller if we adjust the timing offset correctly, but at this point 80ns is small enough for a pre-selection. More study for timing calibration will be reported in chapter 4.

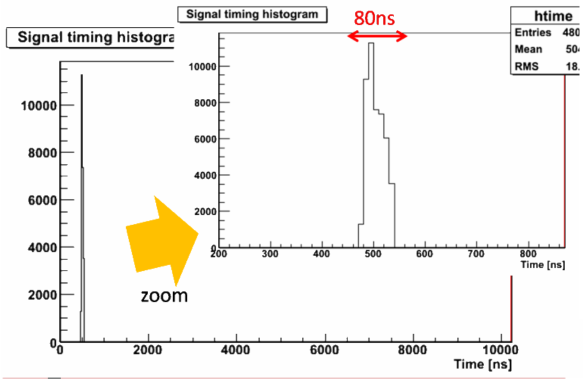

Figure 3.11: Beam timing distribution.

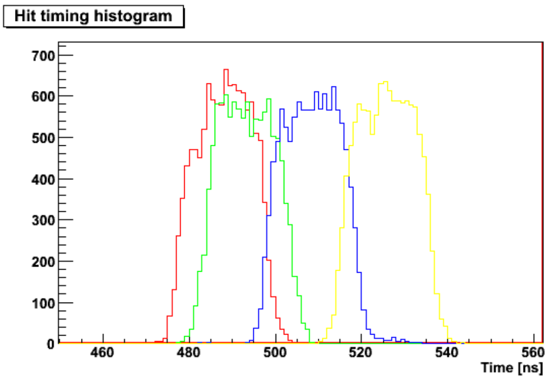

Figure 3.12: Beam timing distribution for 4 crates. Red, green, blue and yellow lines correspond to crate 4, 10, 13 and 19 respectively.

2. Noise threshold PE_{noise}

Second, we determined the noise threshold PE_{noise}. In order to determine this parameter, we checked the efficiency of selecting the particle hits. To do this, we make the particle hit sample and noise hit sample in following ways.

Particle hit sample

Cut the hits below 1.5 p.e. Find the hit position in the first and last layers by selecting the hit which occurred within the beam timing ± 80ns. If there are more than two hits in those layers, select the biggest one. Draw a line which connects these two hits. Then, the particle hit are defined as the hit whose location and timing are in ±3 bars from he line and in the beam timing of ±80 ns, respectively.

Noise hit sample

Select the hit which appeared outside the line ± 3 bars region, or the hit which occurred before/after beam timing of ± 80ns.

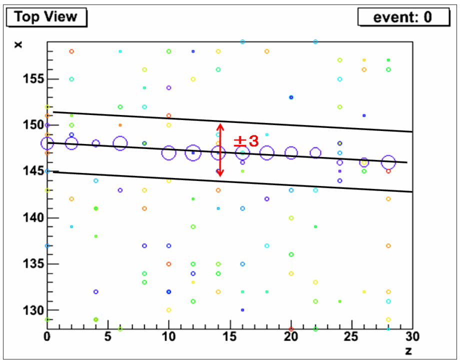

Figure 3.13: Event display of beam track. Size of the circle represents the pulse height, color represents the pulse timing. Three lines shows the region to regard the hit as a particle hit.

For this analysis we set T_{width} as 80ns, and rejected the events which did not have a hit in first or last layers. Figure 3.14 and 3.15 are plots for the number of particle/noise hits vs. noise threshold PE_{noise}.

The expected number of particle hits per event is 30 since we have 30 XY layers and most of the time we have one hit per one layer. From these plots, we determined the PE_{noise} as 2.5 p.e. to keep all the particle hits and eliminate most of the noise hits.

3. Pulse height sum PE_{sum}

Even if the two cuts using T_{width} and PE_{noise} are applied, there are still some cases in which noise hits can survive the cuts:

1. Noise hits above PE_{noise} accidentally appeared within T_{width}.
2. Noise hit appeared within beam timing $\pm T_{width}$. If there is again another noise hit within T_{width} from that accidental noise hit, that hit will be selected in the cluster as well.

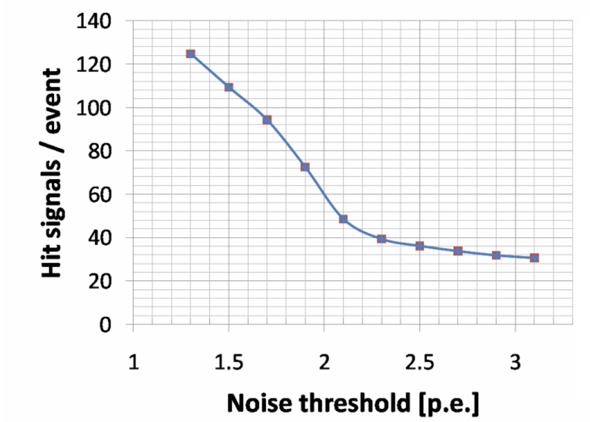

Figure 3.14: Number of particle hits per event vs. noise threshold

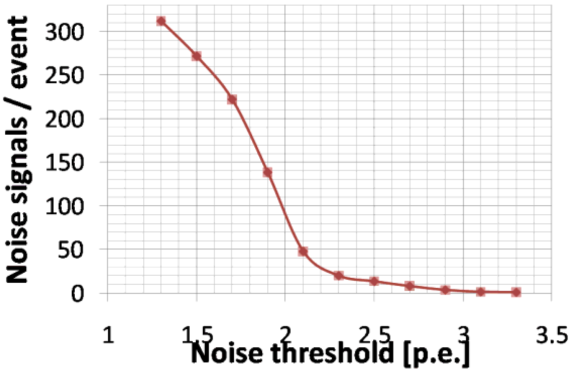

Figure 3.15: Number of noise hits per event vs. noise threshold

Setting the parameter PE_{sum}, we can eliminate most of those hits by requiring the pulse height sum of two hits to be greater than PE_{sum}. To adjust this parameter, we checked the pulse height sum of two hits for particle/noise hits. In each event we selected the particle/noise hits in the same way as we did to determine the parameter PE_{noise}. Then, for all the combinations of two pulses in the particle/noise hits, we calculated the pulse height sum. For this analysis we used the data after the two cuts with T_{width} and PE_{noise} was applied.

Figure 3.16 shows the distribution of pulse height sum for particle hits (red) and noise hits (black). There are two peaks for particle hits corresponding to the pulse

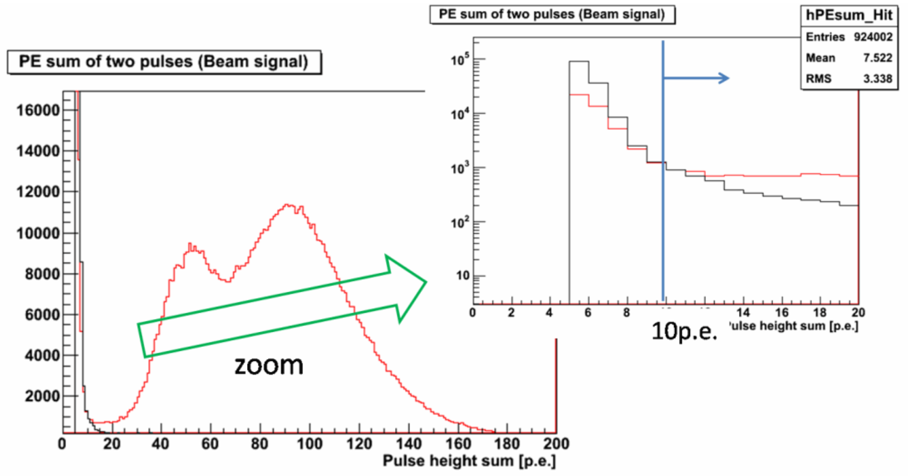

Figure 3.16: Pulse height sum of two pulses for particle hits (red) and noise hits (black).

height sum of (particle hit + particle hit) and (particle hit + accidental noise hit). From these distributions we determined the $PE_{sum} = 10$ p.e. to cut most of the accidental noise hits.

Figure 3.17 ~ 3.20 shows an example of beam triggered event with no cut, only with the PE_{noise} cut, with the PE_{noise} and T_{width} cuts, and with all three cuts. The number of particle/noise hits per event with each cuts is summarized in Table. 3.1.

PE_{noise}	T_{width}	PE_{sum}	Particle hits	Noise hits
-	-	-	626.4	2596.9
2.5	-	-	41.3	28.7
2.5	80ns	-	36.2	13.6
2.5	80ns	10 p.e.	30.7	1.3

Table 3.1: Summary of clustering cut.

With this hit selection cut, we could successfully cut more than 99.9% of noise hits without cutting the particle hits.

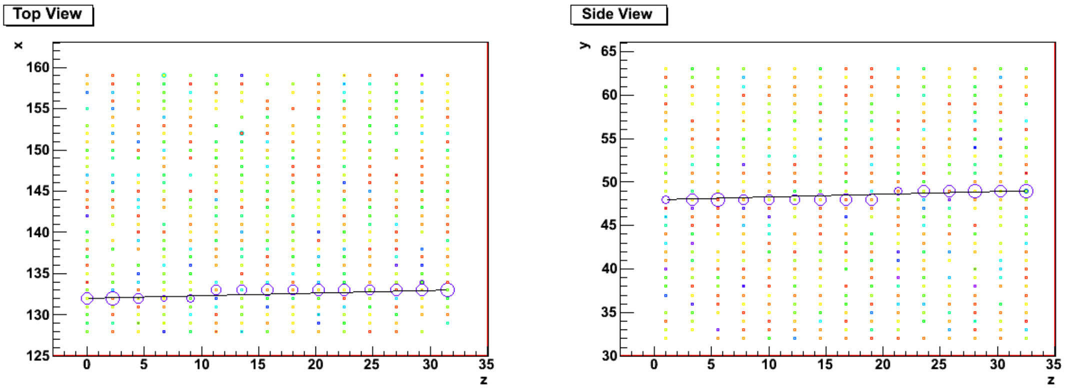

Figure 3.17: Example of event display without any cut.

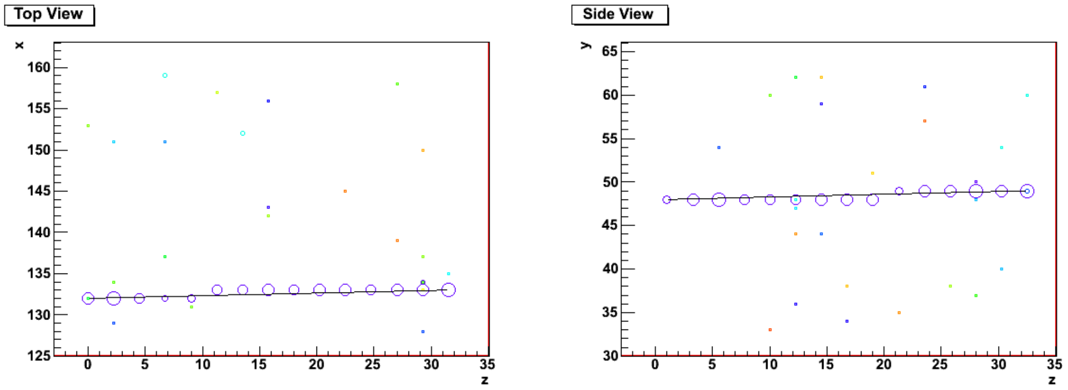

Figure 3.18: Example of event display with 2.5 p.e. threshold cut.

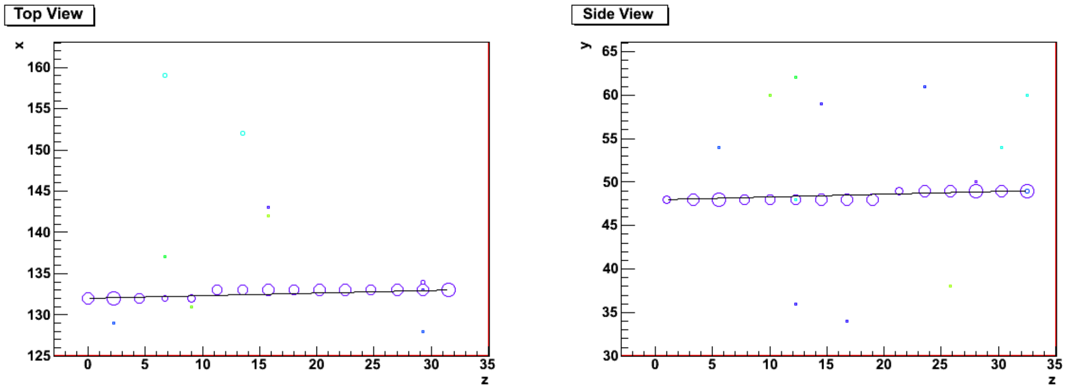

Figure 3.19: Example of event display with 2.5 p.e. threshold and timing cut.

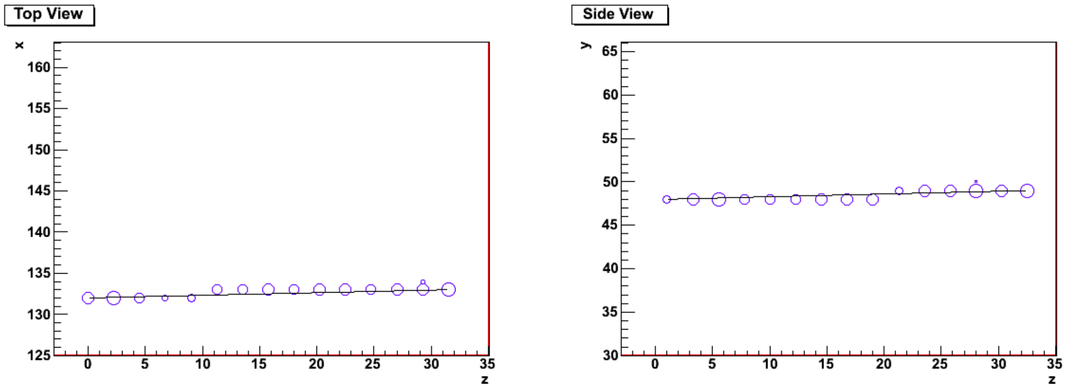

Figure 3.20: Example of event display with all three cuts.

Chapter 4

Commissioning at J-PARC

After the beam test, the FGDs were shipped to Tokai in June and July 2009. They were re-assembled in the assembly building next to the ND280 pit, and installed into the pit in October 2009. Before and after the installation, we took cosmic-ray data to check the detector performance.

In this chapter, we focus on the result of detector performance with cosmic-ray data after reporting the assembly works in the first section.

4.1 FGD reassembly work and installation into the pit

The FGD1 and the FGD2 arrived on June 19 and July 15, respectively. In the following we describe the re-assembly work for both FGDs. The procedure for this work was almost the same for both FGDs.

First, we set the FGD on wooden legs to check if the detector is damaged in the shipment or not.We found that some connectors were loose, but there were no obvious damage to the detector. Then we did a quick check to find dead channels. Figure 4.1 shows the picture of the set up of this test. Since we did not have enough front-end cards (FEBs and CMBs) to install for all the crates, we did the test for crate by crate by using the same cards. For this test, we just simply checked if we see the signal of MPPC's dark noise or not to find bad MPPCs or backplanes. As a result, we found 5 dead channels and 1 bad backplane for FGD1, and 2 dead channels for FGD2. We replaced all of them.

After the quick check, we tilted the FGDs to the vertical to get ready for installation in the pit (Fig. 4.2). Then we installed all the front-end cards to the detector, and connected them to the back-end electronics. We tested the electronics and the detector with noise/cosmic-ray data at this time. We also did the leak test for the water panels before/after stacking them in the FGD2. There were no significant leak observed in any of the panels. Finally, on October 6, we installed two FGDs into the pit. The FGDs were carried by a fork lift from the assembly building to the neutrino

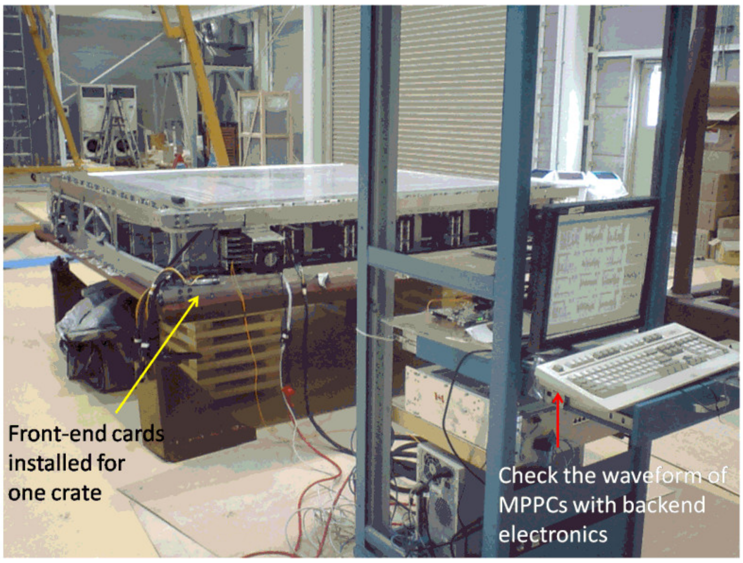

Figure 4.1: Testing the MPPCs crate by crate by using a portable rack.

Figure 4.2: Tilting the FGD to the vertical. All assembly works were done by muscle power.

monitor building where the ND280 pit exists, and craned down by contractors to the ND280 basket (Fig. 4.3). The two FGDs were successfully installed without any accidents. We continued testing the detector with noise/cosmic-ray data in the pit for further study.

Figure 4.3: Installing the FGD. The crane slowly lowered the FGD into the basket.

4.2 Commissioning and performance test

Before and after the installation we tested the detectors and checked its performance to be ready for the neutrino beam run. In this section we report the result of those tests.
To check the performance of the detector, we first checked if all the MPPC channels are working fine (Section 4.2.1). Most of the channels were working fine except for the small number of bad channels.
After this test we measured the breakdown voltage for the MPPCs (Section 4.2.2). We set the bias voltage for MPPCs according to the measured breakdown voltage so that the gain of all the channels will be uniform.
Next, we tested the module called CTM (Cosmic Trigger Module). This module generates the cosmic-ray trigger. We checked the quality of data taken with self cosmic-ray trigger (Section 4.2.3). The CTM also has a function to calibrate the hit timing between the crates. We tested the timing calibration method using this module and measured the timing resolution of the detector (Section 4.2.4).
Finally, we checked the performance of the scintillators bars with cosmic-ray data. We measured the light yield of the scintillators from cosmic-ray data to check the

scintillator's performance (Section 4.2.5). Also we measured the efficiency to find a hit in the scintillator bars when the cosmic-ray passed through the bar (Section 4.2.6).
The items of tests are summarized in Table 4.1.

Tested items	Purpose
Bad channels check	Test if all the channels are working fine
Voltage scan	Set the correct bias voltage for MPPCs
Cosmic-ray trigger quality check	Check the quality of data taken with FGD cosmic-ray trigger
Timing calibration	Test the timing calibration method and check the timing resolution
Scintillator light yield check	Measure the light yield of the scintillator bars for a minimum ionizing particle
Hit efficiency check	Check the efficiency to find a hit when the particle passed through the scintillator bars

Table 4.1: Tested items and purposes

4.2.1 Bad channels check

First we tested all the channels by dark noise hits and cosmic-ray hits to see if they are working correctly. As a result we found < 1% of bad channels which is small enough not to degrade the track reconstruction.

Dark noise test

To find bad channels associated with MPPCs/backplanes/FEBs, we checked the pulse height distribution of the dark noise hits. Figure 4.4 shows an example of pulse height distribution. In addition to the 1 p.e and 2 p.e. peaks, there is a small peak below 1p.e. pulse height which corresponds to so called "pick-up noise". This "pick-up noise" is generated when the temperature of the front-end electronics is high, and it disappeared after we implemented the water cooling system in the ND280 pit.
The over voltage was set to V_{over}=0.85 V for this run, according to the spec sheet provided by Hamamatsu Photonics. We checked the pulse height distribution for all 8448 channels by eye. As a result we found three types of bad channels: "Dead", "Low gain" and "High gain" as shown in (Fig. 4.5, 4.6, 4.7).

Dead: Pick-up noise only (Fig. 4.5). There were 34 channels found.

Low gain: The 1p.e. peak much lower than the usual peak (Fig. 4.6). There were 14 channels found.

High gain: The 1p.e. peak much higher than the usual peak(Fig. 4.7). There were 9 channels found.

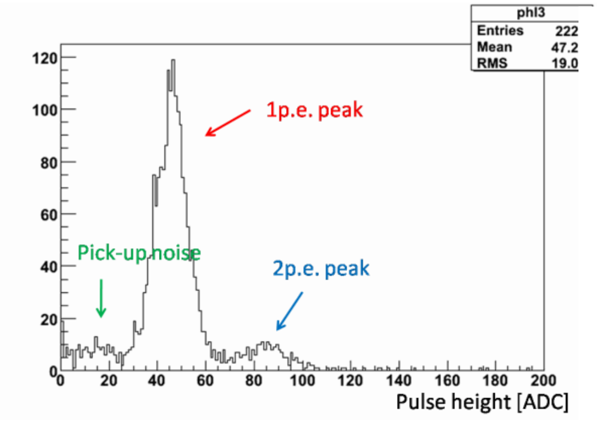

Figure 4.4: Pulse height distribution of dark noise pulses (Normal channel)

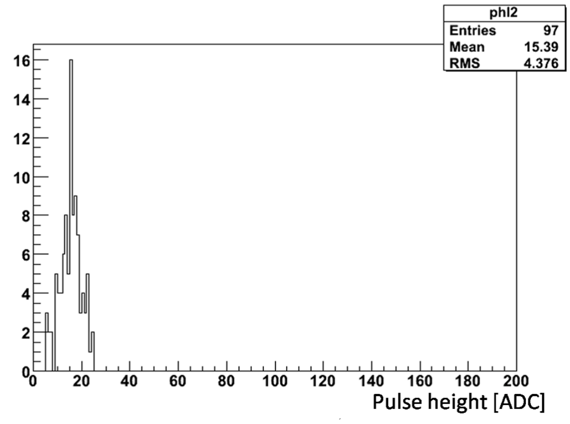

Figure 4.5: Pulse height distribution of "Dead" channels

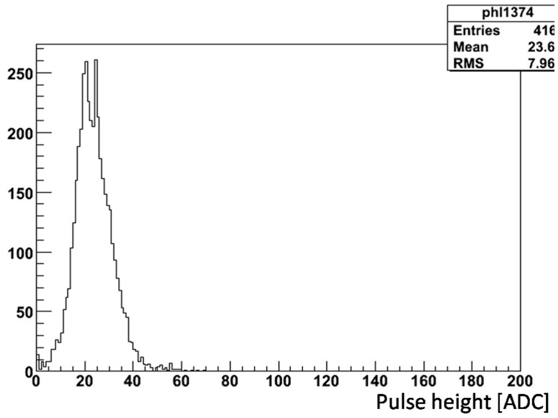

Figure 4.6: Pulse height distribution of "Low gain" channels

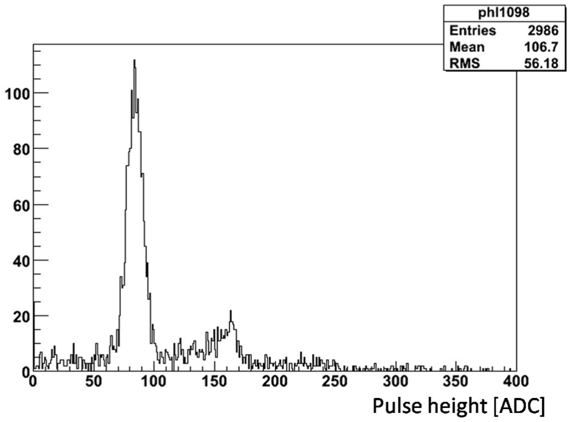

Figure 4.7: Pulse height distribution of "High gain" channels

As for "Low gain" channels and "High gain" channels, the bias voltages are apparently wrong. If the serial number of that MPPC is wrongly recorded in the database, these channels will have wrong bias voltage. However there were no way to check it since we already closed the FGD dark box. We measured the correct bias voltages for these channels by taking "voltage scan" run (see section 4.2.2) and they work fine after setting the correct bias voltages.
It was surprising that we found many more of "Dead" channels than we found in

the initial test before tilting the FGDs. One possible explanation for this problem is that these bad channels are associated with the FEBs that we installed after the initial test. In the initial test, we did the test for crate by crate using the same set of FEBs. We did the installation of FEBs after tilting the FGDs to the vertical, and those FEBs might contain some bad channels on it. Therefore we swapped the FEBs to see if the "Dead" channels move. As a result we found 18 of them actually moved by swapping the FEBs, so these channels have a problem on the FEB. The 6 "Dead" channels were removed by swapping the FEBs. However, since we only had two spare boards, we did not have chance to remove all of them. Additional spare FEBs are already ordered and will be installed the next time when we have an access to the detector.

Currently we have 37-6 = 31 "Dead" channels, but 31/8448 = 0.37% is small enough to reconstruct the particle tracks with high efficiency. We recorded the location of those "Dead" channels in the database.

Light yield check

We also checked the light yield of scintillators by cosmic-rays data to find bad channels associated with a bad scintillator/fiber. Since the module to generate the cosmic trigger was not implemented until we started the FGD2 cosmic test, we initially used the external scintillator trigger for the FGD1 cosmic-ray test. Figure 4.8 shows the setup for cosmic-ray test when we tested the FGD1. We moved the trigger scintilla-

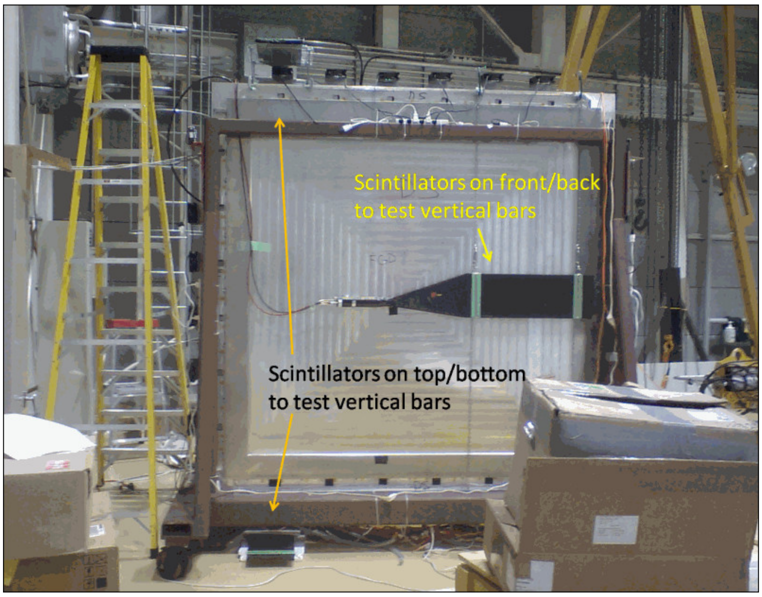

Figure 4.8: FGD1 from down stream side. We hanged 2×2 scintillators on the front/back side of the FGD when we tested the vertical bars, and placed at the top/bottom of the FGD when we tested the horizontal bars.

tor in the horizontal direction to test all the bars. Bias voltage for MPPCs were set to $V_{over} = 1.05V$ according to the spec sheet provided by Hamamatsu Photonics. Figure 4.9 shows a pulse height distribution of cosmic-ray hits. We checked the shape of pulse height distribution for all 8448 channels by eye to find bad channels. Except for the bad MPPC channels found in the dark noise test, we found additional 27 bad channels whose pulse heights were much lower than that of the normal channel (Fig. 4.10). We assumed that these channels are corresponding to bad fiber coupling with MPPCs. However it was impossible to open the FGD and fix the fiber at that time with the FGD tilted to vertical. Therefore we decided to leave them as they are and record the location of bad channels in the database.

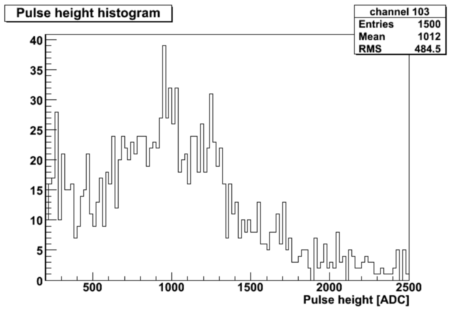

Figure 4.9: Pulse height distribution (Normal channel)

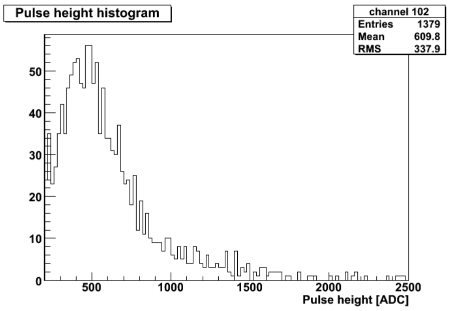

Figure 4.10: Pulse height distribution (Bad channel)

To summarize, currently we have 31 dead channels and 27 low pulse height channels. Of the dead channels, 18 are expected to be fixed by replacing the FEBs. The total number of bad channels is smaller than 1%. This is small enough not to degrade reconstructing a particle track from neutrino interaction, and thus the quality of our detector is good enough.

4.2.2 Voltage scan and breakdown voltage measurement

In the bad channels test we found that some channels had the wrong bias voltage applied. It is also possible that there are more channels with wrong bias voltage but were not found in the bad channels test because they were not significantly wrong. Therefore it is necessary to re-measure the breakdown voltage on the detector and apply the correct bias voltage instead of using the spec sheet provided by Hamamatsu Photonics.

We took a "voltage scan" run to derive the correct bias voltage. The method to get the correct bias voltage by "voltage scan" is following:

1. Take periodically triggered runs in several different bias voltages (these runs are called as voltage scan).

2. For each run, make a pulse height distribution and derive the 1p.e. pulse height (=gain) from the first peak.

3. Make a plot of bias voltage vs. 1p.e. pulse height (Fig. 4.11). Since the gain increases linearly as the bias voltage increase, we can derive the breakdown voltage by fitting the plot with a straight line and by extrapolating the voltage where the 1p.e. pulse height becomes 0.

4. Set the bias voltage as breakdown voltage + constant value.

Figure 4.12 shows the the breakdown voltage derived by this method for 8448 channels. Breakdown voltages are much different between different channels corresponding to different wafer used to produce the MPPCs.

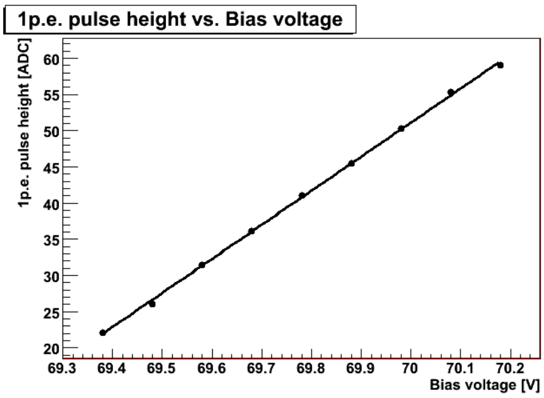

Figure 4.11: 1p.e. pulse height vs. Bias voltage

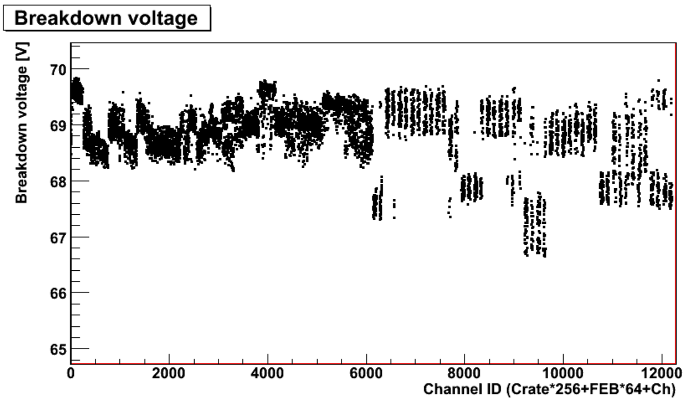

Figure 4.12: Breakdown voltage vs. channel ID

Figure 4.13 and 4.14 show the plots of gain vs. channel ID, for when we set the bias voltage according to the spec sheet provided by Hamamatsu Photonics (Fig. 4.13) and for when we used the bias voltage derived from voltage scan data (Fig. 4.14). When we set the voltage according to Hamamatsu spec sheet, the gain was not uniform between the channels. This is because the temperature was higher for the channels with small channel IDs, and lower for the channels with big channel IDs. The gain were much uniform when we used the bias voltage derived from the voltage scan data.

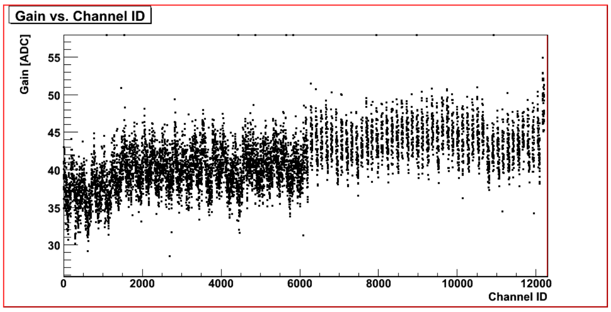

Figure 4.13: Gain vs. channel ID with the bias voltage derived according to the spec sheet provided by Hamamatsu Photonics. The gain was affected by the temperature.

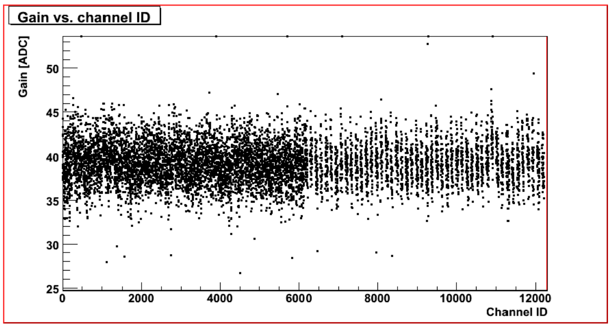

Figure 4.14: Gain vs. channel ID with the bias voltage derived from the voltage scan.

The breakdown voltage values are recorded in the database together with the temperature value at that time. For continuous data taking, we will check the temperature periodically and apply a correction according to the temperature effect. This procedure is now under discussion.

4.2.3 Cosmic trigger quality check

Cosmic-rays will be used for detector calibration, for example, to measure the photoelectron yield for minimum ionizing particles. In order to take data with cosmic-rays,

we developed CTM (Cosmic Trigger Module) which will generate cosmic triggers. We checked the quality of the data taken with cosmic-ray trigger generated by this module.
The CTM is connected to all the CMBs (Crate Master Boards) and makes a decision to generate a trigger according to the trigger condition (Fig. 4.15). We aim to detect the cosmic-rays which pass through both the FGD1 and the FGD2 (Fig. 4.16). The cosmic-ray trigger is generated in two steps. First, the CMB provides the trigger primitive according to the trigger condition in the CMBs. Second, the CTM decides to generate the cosmic-ray trigger when the specific combination of CMBs are triggered.
The CMBs provide the trigger primitive when the following condition is fulfilled:

1. All the channels in the crate are grouped in sets of eight. We call the group of 8 channel as "ASUM group". The 8 channels correspond to half the channels in one layer, since one crate reads out 16 channels from each layers.
2. Signals from the 8 channel are summed up in each ASUM groups. The ASUM group provides a signal to the CMB when the summed up signal gets higher than the threshold.
3. CMB collects the signals from ASUM groups and decide to provide the trigger primitive when more than 2 ASUM group fired at the same time.

Then the CTM decides to generate a cosmic-ray trigger according to the following condition:

((Any CMB in FGD1 X) && (Any CMB in FGD1 Y))
&& (((Any CMB in FGD2 X) && (Any CMB in FGD2 Y))

In order to check what kind of tracks are selected by this trigger requirement, we checked the number of hits in each scintillator bar in the cosmic-ray triggered data. In this analysis, cosmic-ray hits were selected by the following way:

1. Cut the dark noise hits by the time clustering method explained in section 3.3.
2. Convert the hit channel ID to the actual position in the detector. From the array of coordinates, calculate the slope and intercept of the linear fit function by using the least square method.
3. Reject the hits which are too far from the fitted line. For each hit, calculate the square of the residual from the fitted line.
   $(Residual)^2 \equiv (Bar_{fitted} - Bar_{data})^2$
   Find the point where $(Residual)^2$ is maximum. If $(Residual)^2_{max} > 4$ (more than 2 bars separated), reject that point and fit again.

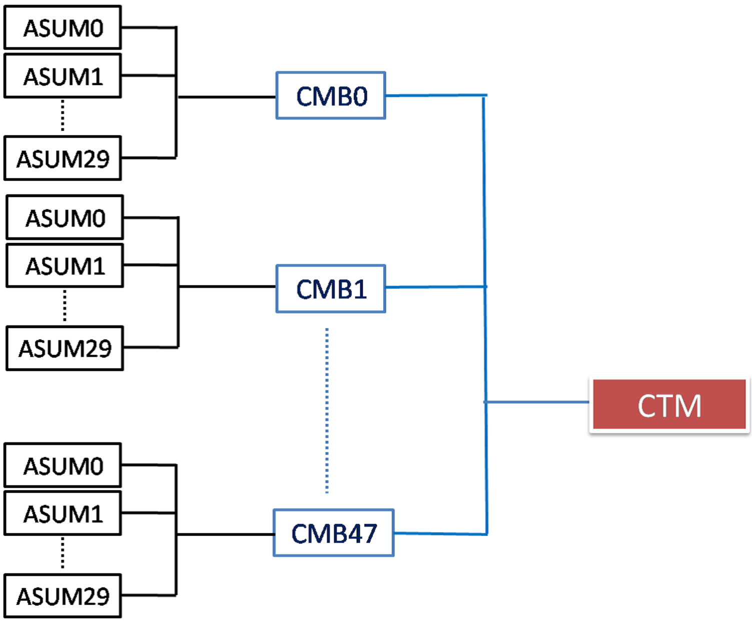

Figure 4.15: Diagram to define cosmic trigger condition.

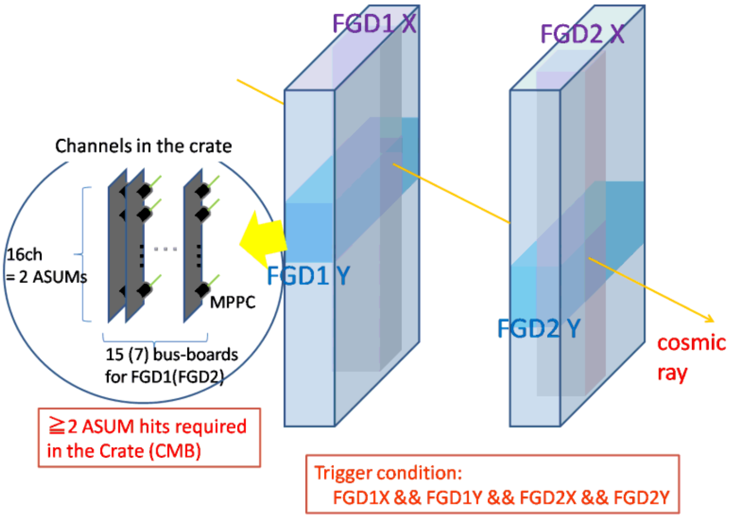

Figure 4.16: Concept of cosmic-ray selection. The trigger is generated when there are hits in both FGD1 and FGD2, for X(vertical) and Y(horizontal) bars.

4. Continue fitting until $(Residual)^2_{max}$ gets lower than 4. Select the hits which survived in the track as cosmic-ray hits.

We fitted the points in each FGD independently, since the two FGDs are not perfectly aligned. Figure 4.17 shows an example of cosmic-ray triggered event. The CTM is selecting a good cosmic-ray track and the fitting line is correctly calculated by this method. As a result, Fig. 4.18 $\sim$ 4.21 shows the distributions of number of hits which survived this selection, and Fig. 4.22 shows the angular distribution of the tracks. In Fig. 4.18 $\sim$ 4.21, the horizontal axis corresponds to XY module(plane) IDs, and the vertical axis corresponds to the scintillator bar IDs. The module IDs are assigned from 0 (0) to 14 (6) for FGD1 (FGD2) from upstream to downstream. For the vertical bars, the bar IDs are assigned from 0 to 191 from the right side to the left side, looking downstream. For the horizontal bars, the bar IDs are assigned from 0 to 191 from the bottom side to the top side. The color represents the number of hits in that bar. As we see from Fig. 4.20 and Fig. 4.21, the tracks which entered from the top of FGD1 and the bottom of FGD2 are more common than the tracks which entered from the top of FGD2 and the bottom of FGD1. The reason for this bias is under investigation.

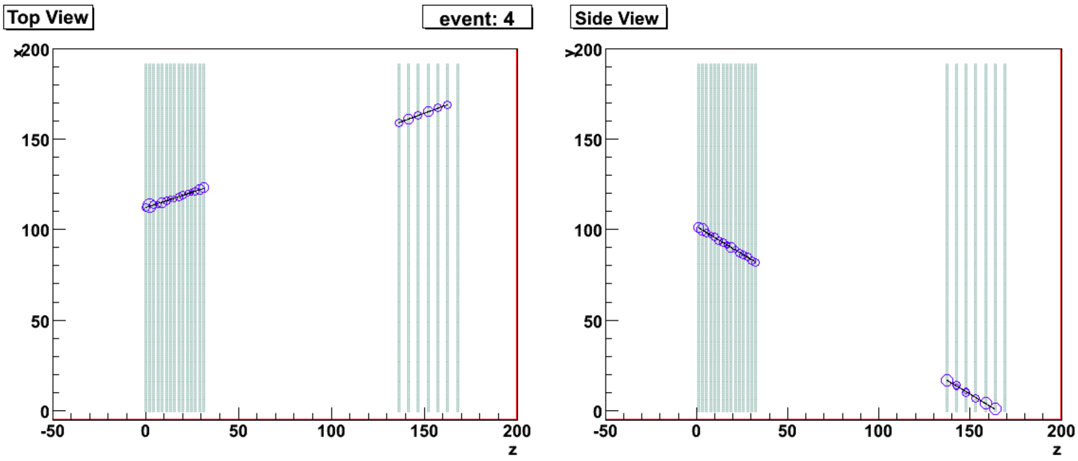

Figure 4.17: Examples of event display of cosmic-ray events. Points are fitted by the straight line using least square method. Radius of each circle corresponds to the pulse height of that signal, and the color corresponds to the timing.

There is a “stripe” pattern seen especially in FGD2 X. This is because the CMBs require $\geq$2 ASUM group hits which in principle means $\geq$2 layers hits in the same crate are required. Because of this condition, the tracks which passes $\geq$2 layers in the same crate are enhanced. To summarise, the CTM is correctly working to select the cosmic trigger, and the bias of the trigger is measured.

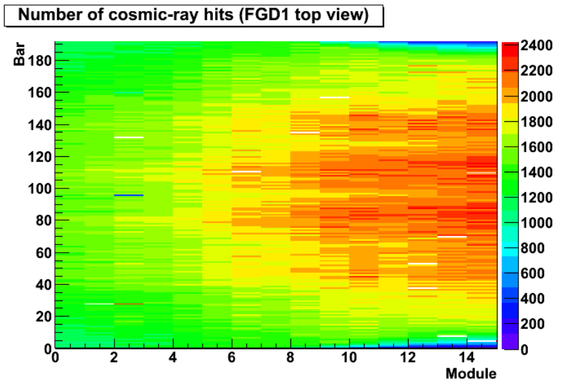

Figure 4.18: Number of hits in FGD1 (top view)

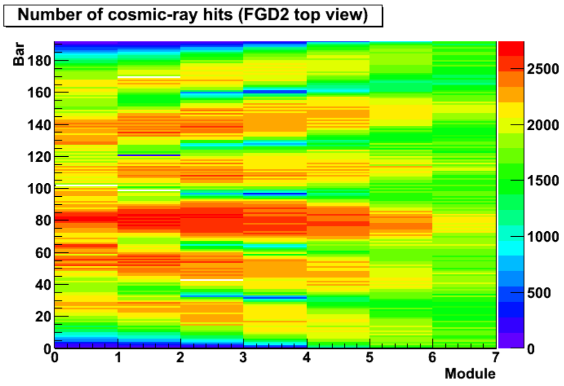

Figure 4.19: Number of hits in FGD2 (top view)

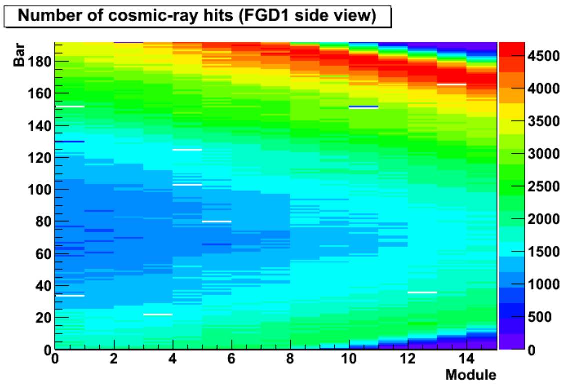

Figure 4.20: Number of hits in FGD1 (side view)

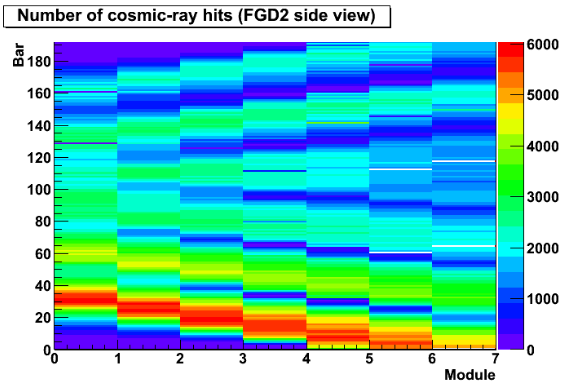

Figure 4.21: Number of hits in FGD2 (side view)

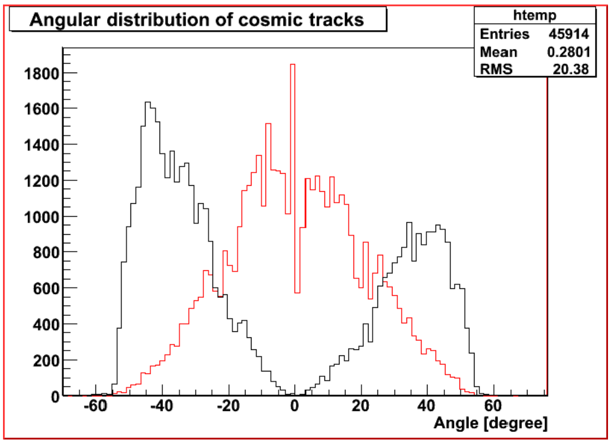

Figure 4.22: Angular distribution of cosmic tracks. Red(Black) line corresponds to the distribution in X(Y) projection.

4.2.4 Timing calibration

In order to combine the hits from neutrino interaction with the other ND280 detectors, we use the timing information as well as topological information. The requirements for the timing resolution is approximately 3 ns per neutrino interaction to reject background hits. The CTM has a function called "Timing Marker" to measure the time offset in the readout electronics for the crates. We tested this function and measured the timing resolution of the detector.
There are several sources in the readout electronics which generate time offsets. They are shown in Fig. 4.23. In this diagram, each squares represents the modules in the readout electronics:

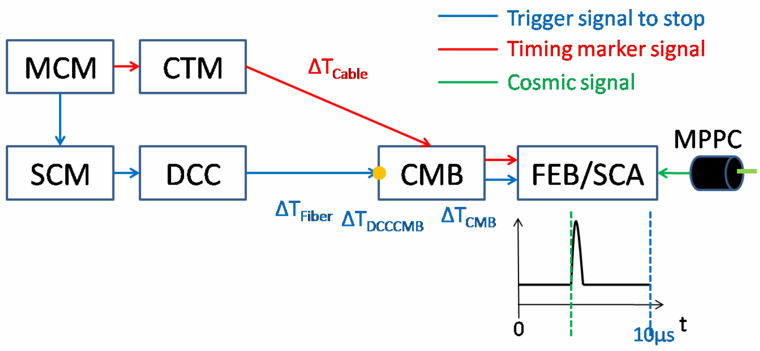

Figure 4.23: Overview of FGD readout electronics.

- MCM (Master Clock Module): Distributes the trigger timing for the near detectors.

- SCM (Slave Clock Module): Receives the trigger from MCM and distributes to the DCCs.
- DCC (Data Concentrator Card): Collects the data from the crates and pass them to the DAQ system.
- CTM (Cosmic Trigger Module): Provides the cosmic trigger.

These 4 modules are the back-end modules. The CMB (Crate Master Board) and the FEB (Front End Board) are the front-end modules. The SCA (Switched Capacitor Array) on the FEB continuously records the waveform until the trigger signal arrives from the MCM. The source of time offset exists in this trigger signal line. As described in the figure there are three different sources which generates the time offset: $\Delta T_{fiber}, \Delta T_{DCCCMB}$ and ΔT_{CMB}.

- ΔT_{fiber}: Propagation delay of the optical fiber cable which connects the DCC and CMB. ΔT_{fiber} is less than ∼30ns.
- ΔT_{DCCCMB}: Phase shift between the clocks of the back-end modules and the front-end modules. This time offset changes between 0∼10ns whenever we power up the modules.
- ΔT_{CMB}: 0ns or 10ns jitter between the CMB clock (100MHz) and SCA clock (50MHz). It changes in each event.

Time offset is the sum of these three. “Timing markers” were implemented in the CTM to measure the time offset in the readout electronics and to synchronize the timing between the crates.

The method to measure the time offset by timing marker is the following:

1. The CTM sends the pulse signals to all the FEBs at once via CAT6 cables. This signal is called “timing marker”.
2. Then the time we read out from the timing marker signals is different between the crates due to the time offsets in the readout electronics and CAT6 cable propagation delay.

   $$\begin{aligned}&\text{Timing difference between the timing markers}\\ &\qquad\qquad = \text{Time offset} + \text{Cable delay(CTM-FEB)}\end{aligned}$$

3. The cable propagation delay can be calculated from the cable length (5.4ns/m). Therefore, we can measure the time offset in the readout electronics by subtracting the CAT6 cable propagation delay time from timing difference between the markers.

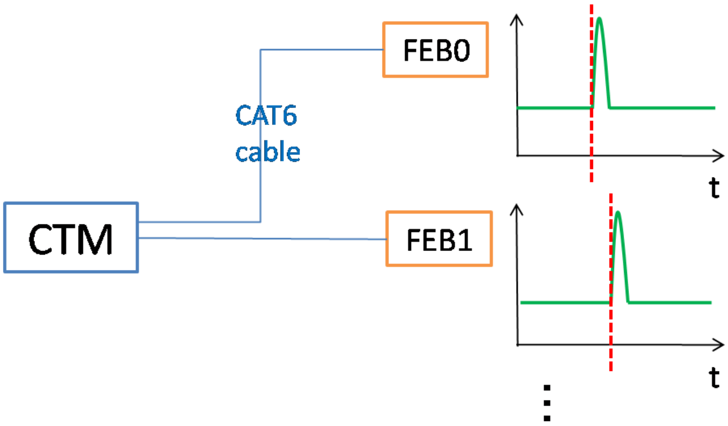

Figure 4.24: Timing marker system. CTM sends the signal to all the FEBs at the same timing via CAT6 cables.

We tested this method with the cosmic-ray data. For each FEBs, we calculated the time offset with respect to Crate0 FEB0 and the corrected hit timing:

$$\begin{aligned}\text{Corrected marker timing} &= \text{Measured marker timing - (CAT6 cable length [m]}\\ &\quad \times \text{Propagation delay [ns/m])}\end{aligned}$$

$$\begin{aligned}&\text{Time offset with respect to Crate0 FEB0}\\ &\qquad = \text{Corrected marker timing for the FEB of interest}\\ &\qquad\quad \text{- Corrected marker timing of Crate0 FEB0}\end{aligned}$$

$$\text{Corrected hit timing} = \text{Raw hit timing - Time offset.}$$

First, we checked the RMS of cosmic hit timing in each events. To select the cosmic-ray hits, we used the time clustering method as explained in section 3.3. In Fig. 4.25, the black(red) line shows the RMS of hit timing before(after) correction. For this check we checked the RMS of hits in FGD1 and FGD2 separately because the hit timing is different between the two FGDs due to the time of flight between the two detectors. The RMS became much smaller after synchronization. From the mean of the RMS distribution, the timing resolution of the detector is 4.9ns. This is close to the required resolution, but slightly worse. Figure 4.26 and 4.27 show the mean timing of cosmic-ray hits in the crates before and after correction. The range of the vertical axes are same for both plots. The deviations of of the timing are much smaller after correction, but not perfect.

The two FGDs are ~1.3m separated, so the time of flight between two FGDs are expected to be ~5 ns. If the particle passes through both FGDs and timing resolution is good enough, we can distinguish the particle direction by comparing the hit timing

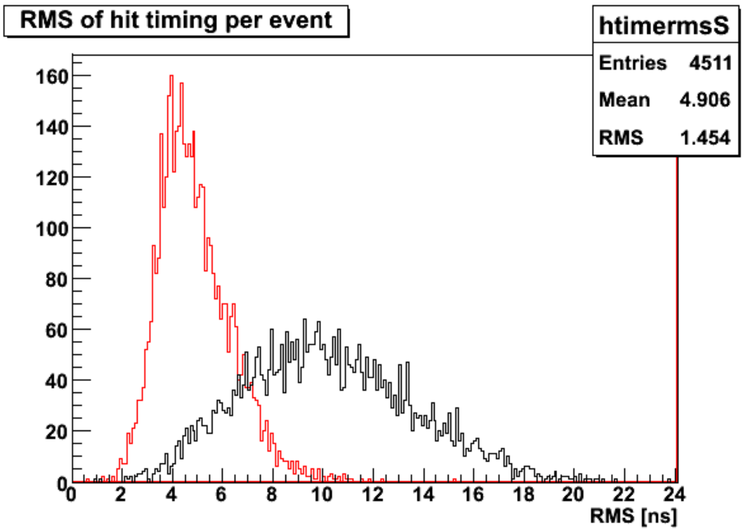

Figure 4.25: RMS of signal timing per event

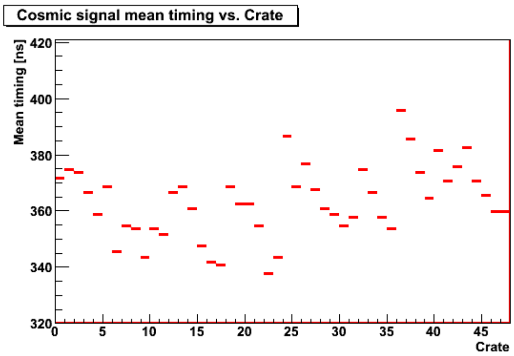

Figure 4.26: Mean timing of cosmic-ray hits for crates (Before correction)

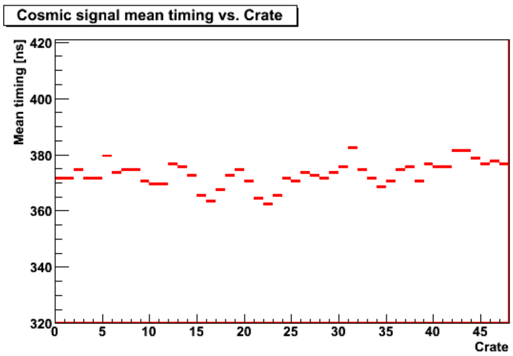

Figure 4.27: Mean timing of cosmic-ray hits for crates (After correction)

between two FGDs. We tested this method in the cosmic-ray data by looking the difference of mean timing of hits in each FGDs and comparing it with the cosmic track angle.

First we fitted the cosmic track by using the same method we used in section 4.2.3. From the fitted line, we calculated the track angle in Y-Z projection and made a plot of the difference of mean hit timing between two FGDs vs. track angle. Fig. 4.28 shows the result. In this plot the positive angle corresponds to the track from FGD2 top to FGD1 bottom, and vice versa. Since the timing synchronization is not perfect, this plot in not symmetric in vertical direction and shifted down wards by ~3 ns. We could clearly separate the track direction by the hit timings between two FGDs.

We achieved 4.9 ns timing resolution by correcting the timing with timing marker. This is slightly worse than required, but good enough to determine the direction of track which passes through both FGDs. This will be invaluable for discerning backwards-going tracks in the Tracker.

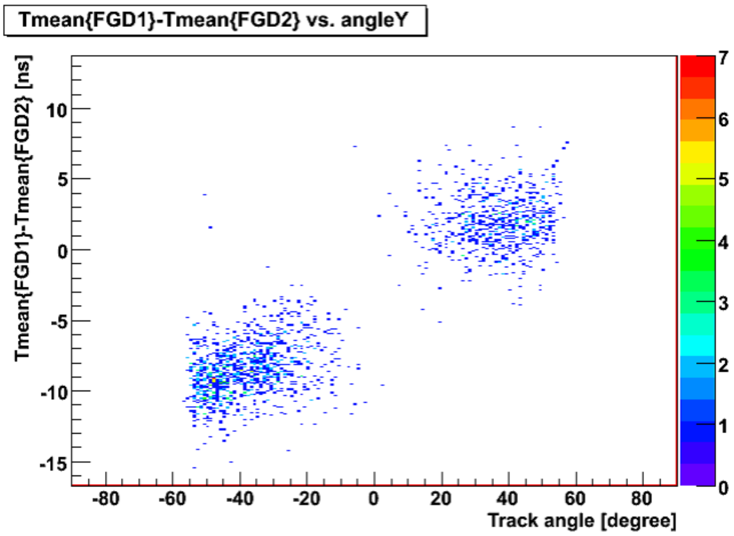

Figure 4.28: Difference of mean timing in two FGDs vs. the track angle.

4.2.5 Photo-electron yield per path length

When a minimum ionizing particle passes through the bars, photo-electron yield in the scintillators is expected to increase linearly as the path length increases. We checked this feature from cosmic-ray run data. To derive the path length in the plane, we fitted the track again with the least square method, and derived the formula below:

$$\text{Deposited energy per plane} = \text{Total photo-electron yield of the hits in the track} \\ \div (\text{Number of planes passed} \times \text{Path length per plane}),$$

$$\text{Path length per plane} = \sqrt{1^2 + \text{slopeX}^2 + \text{slopeY}^2},$$

where slopeX and slopeY represent the slopes from fitted line in X projection and Y projection.

The result is shown in Fig. 4.29. Good correlation was seen for deposited energy per plane and path length as expected.

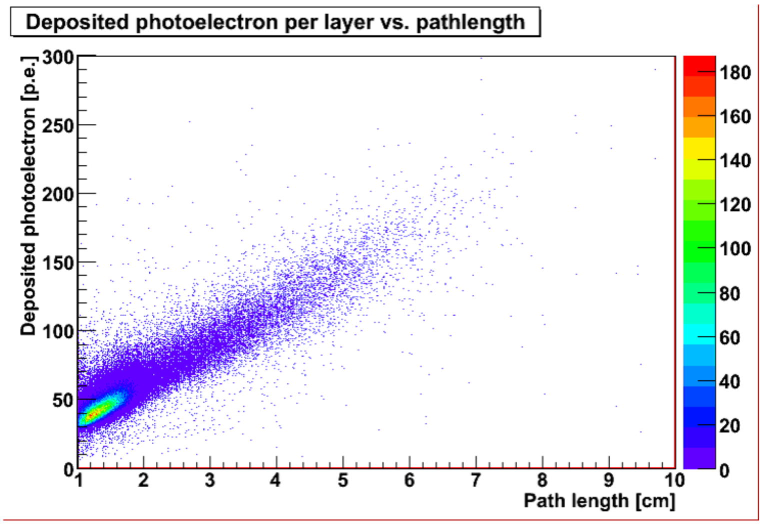

Figure 4.29: Deposited energy per plane vs. path length in the layer.

4.2.6 Hit efficiency of scintillator layers

"Hit efficiency" is the efficiency to find a hit when the charged particle passes through the scintillator layer. If the efficiency is > 99%, the number of missing hits is negligible. The scintillator bars with fibers are designed to make the efficiency better than 99%.

We checked the efficiency of scintillator layers in the cosmic-ray data by the following way:

1. We select the cosmic-ray hits by time clustering cut (section 3.3).
2. Then we fit the track by the least square method. We reject the hits by the same method as we did in section 4.2.3. If the the residual of the hit position from the fitted line is more than 1 bar, we reject that hit and fit again.
3. For the surviving hits, we apply the final fit by the weighted least square method. In this method, we defined the chi-square as following.
   $$\chi^2 = \Sigma(Bar_{fitted} - Bar_{data})^2/PE_{data},$$
   where PE_{data} is the photo-electrons of each hit.

4. According to the fitted line, we determined the position in the layer where we expect to see the particle hits. Then the hit efficiency is calculated as following:

   $$\text{Hit efficiency} = N_{hit}/N_{passed},$$

   where N_{hit} is the number of events that we actually found the hit around the expected position ±1 bar. N_{passed} is the number of events that we expected to find the hits in that layer. If the bar at the expected position contained the dead channel, do not count the N_{passed} for that event.

We did the fitting separately for FGD1 and FGD2, as in section 4.2.3.
Sometimes the fitting failed when the particle trajectory was not a simple straight line. For example, there are following case when the fitting fails:

- Cosmic ray created a shower. (Fig. 4.30)
- Secondary tracks generated. (Fig. 4.31)
- Accidental noise signal appeared in the same cluster. (Fig. 4.32)
- Track was not straight. (Fig. 4.33)

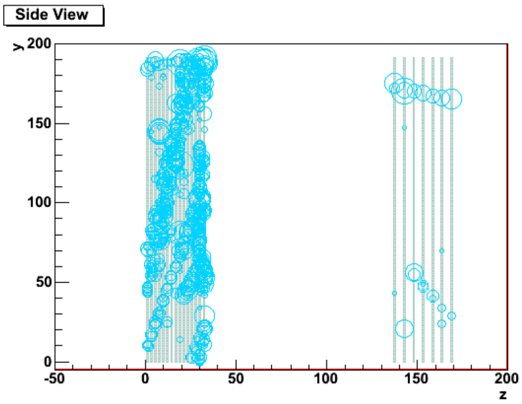

Figure 4.30: Example of shower event.

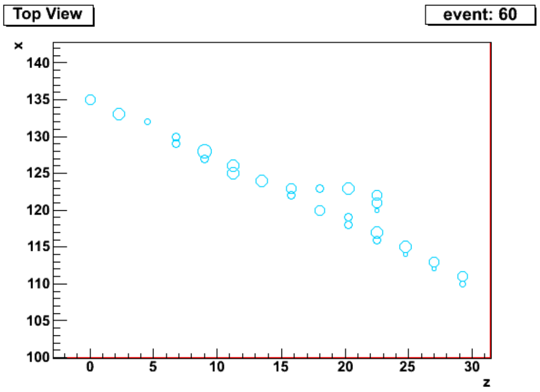

Figure 4.31: Example of secondary track.

In order to reject those events, we applied the cuts below:

- If there were more than 3 hits rejected in the second step of the method above, do not use that event. We can reject cosmic showers or secondary tracks by requiring this condition.
- For the slope of fitted line for FGD1 and FGD2, if the difference of the slope value is greater than P_{diff}, reject the event. The tracks associated with accidental noise hits and the non-straight tracks are rejected by this cut.

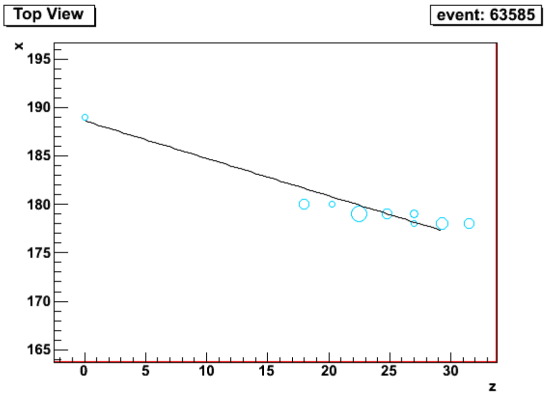

Figure 4.32: Example of accidental noise hit.

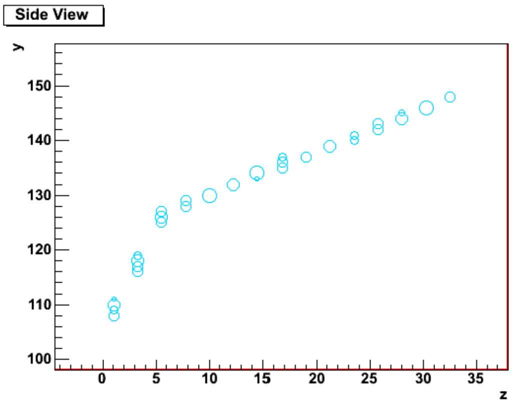

Figure 4.33: Example of un-straight track

To determine the parameter P_{diff}, we checked the distribution of the difference of the slope value between two FGDs (Fig. 4.34).

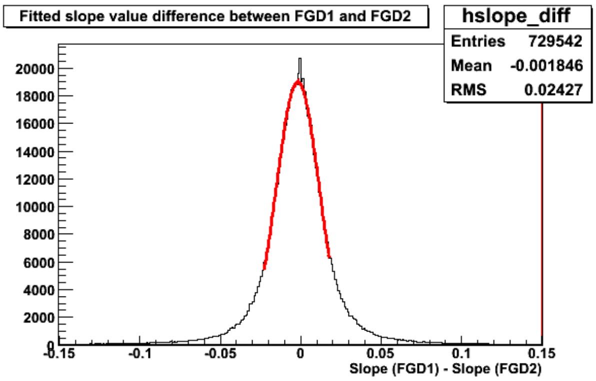

Figure 4.34: Difference of the slope value of the fitted line between two FGDs. The red line shows the fitted line with Gaussian.

We fitted the distribution by Gaussian and defined the parameter $P_{diff} = 2 \times$ sigma ~ 0.026.
For the events which survived the cuts, we checked the hit efficiency.
However, even for the straight track events, we found that fitting is not perfect. For some specific layers, we always found the hit above the fitted line, while for another specific layers we always found the hit below the fitted line. This suggests that the scintillator layers are not aligned perfectly. To correct this effect, we did the following:

1. For every hits, measure the residual from the fitted line, and calculate the mean of the residuals for each layers.

2. Correct the bar position as

   Corrected position = Original position + Mean residual

   for each layers. Fit the tracks with corrected position, and measure the mean of the residuals again.

3. Repeat this procedure for several times until the absolute value of residual gets smaller than 0.1 mm.

Figure 4.35 shows the measured residual for 44 layers before/after this correction. The black points shows the residuals before the correction, while the red points shows the residuals after the correction. Initially there were ∼ ±0.5 mm of residuals, but after the correction the absolute residuals are < 0.1 mm.

Finally we measured the hit efficiency of scintillator layers. The result is shown in Fig. 4.36. The hit efficiency for the scintillator layers were > 99% for all the measured layers. The mean hit efficiency was 99.7%.

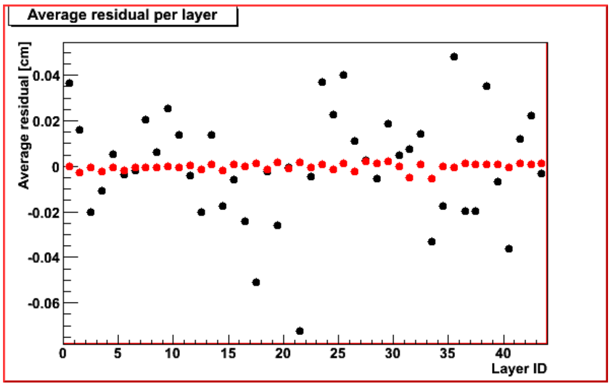

Figure 4.35: Mean residual for 44 layers, before(black) and after(red) the correction.

The even number of layer IDs corresponds to the X layers (vertical bars) and the odd number of layer IDs corresponds to the Y layers (horizontal bars). The hit efficiency was higher for the Y layers that for the X layers. This can be explained from the difference of angular distribution of the cosmic-ray tracks, and from the structure of the scintillator bars. Since the scintillator bars are coated with TiO_2, they are inactive at the edge. We measured the hit efficiency as the function of the distance from the center of the scintillator bar (Fig. 4.37). The hit efficiency becomes much lower at the edge of the scintillator bar.

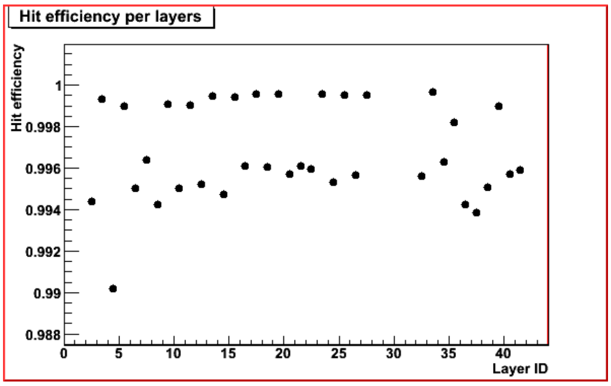

Figure 4.36: Hit efficiency of the layers.

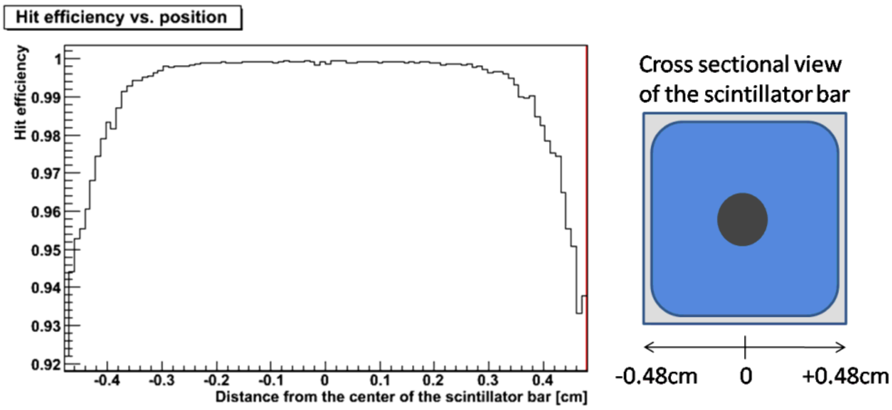

Figure 4.37: Hit efficiency in the function of the distance from the center of the scintillator bar.

If the track angle is small, the particle can pass through the inactive area. According to the angular distribution of cosmic-ray tracks measured in section 4.2.3, the typical track angle is small for the X layers, while it is big for the Y layers. This is why the hit efficiency was higher for the Y layers and lower for the X layers. This indicates that the hit efficiency is dependent on the track angle. The expected angular distribution of the muons generated from the neutrino interaction at the near detector is shown in Fig. 4.38 [10]. The angle is more widely distributed than the cosmic-ray tracks in X layers. Therefore we expect that the hit efficiency is better for the muons from neutrino interactions than that we measured in cosmic-ray data for X layers. We confirmed that the hit efficiency for the muons from neutrino interactions is >99%.

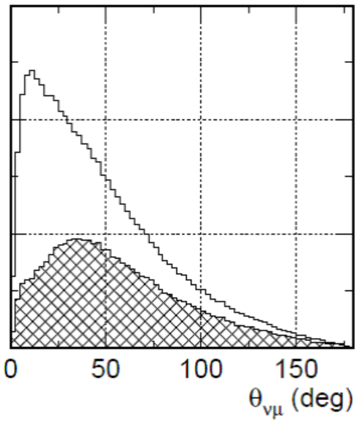

Figure 4.38: The expected angular distribution of muons at the near detector. The shaded region in this distribution represents the angular distribution of muons from CCQE interaction [10].

4.3 Summary of the commissioning and tests before the beam run

The FGDs were re-assembled and successfully installed in the ND280 pit without any accidents. We tested the detector before/after the installation and checked its performance.

Channel test and voltage setting

All the MPPC channels were tested and worked fine except for $< 1\%$ of dead channels and the channels with low light yield. The breakdown voltage for the MPPCs were measured in the voltage scan test in order to apply the correct bias voltage.

CTM test

We tested the cosmic-ray triggering with CTM. It worked fine and the quality of data produced by the CTM trigger is verified.

Timing synchronization method was tested by using the timing marker signals from the CTM, and we achieved the 4.9 ns timing resolution.

Scintillator performance check

Photo-electrons light yield for the minimum ionizing particle were measured as the function of path length. Also we checked the hit efficiency of the scintillator layers, and confirmed that it is $> 99\%$.

All the hardwares and softwares were tested, and the performance were measured. With this condition, we launched into the neutrino beam run.

Chapter 5

Beam commissioning

The neutrino beam run with the FGDs took place in December 2009. At this time most of the ND280 detectors were ready for beam commissioning though the magnet yoke was not closed. We successfully observed the neutrino candidate events in the run and confirmed that the detector is working correctly to measure neutrino events. We also measured the timing of neutrino events to check if they appears at the time we expect from the beam trigger timing. In this chapter we report the summary of two beam runs taken in December and the result of neutrino event observation.

5.1 Summary of the beam run

We took two neutrino beam runs in December 2009. The first beam run took place in Dec 12∼14, and the second beam run took place in Dec 18∼21. The three electromagnetic focusing horns were off for the first run and on for the second run. The beam power was much higher for the second run. Condition of the beam for these two runs are summarized in Table 5.1.

Date	Proton on Targets	Total number of spills	Horn
Dec 12∼14	5×10^{14}	1025	Off
Dec 18∼21	1×10^{16}	7453	On

Table 5.1: Summary of December neutrino beam run

The neutrino beam has a bunch structure. For this run, the number of bunches in the spills were different shot-by-shot, but most of the time it was 1 or 6. The bunches were separated by 581ns from each others.
For the DAQ setup, we took the data with the combination of beam trigger and the 0.13Hz periodic trigger. The periodic trigger was implemented for calibration and background study. The periodic trigger rate was set to be very low since we had a

trouble in the DAQ when we ran with high trigger rate. Also we discarded 99.9% of dark noise hits at this time for data reduction. Therefore we did not have enough data for calibration and it was difficult to find the hits of 1p.e pulse-height. Hence in the following analysis we used the value of calibration constant 0.02 [p.e./ADC] to convert the pulse height to photo-electron.
In these conditions of the beam and DAQ, we searched for the neutrino events.

5.2 Detection of neutrino events

We searched for neutrino events in the two beam runs. The goal of this analysis is to detect neutrino events and compare its timing with the expected timing from the beam trigger timing. We expected to see the particle tracks from neutrino interaction, especially the muon track from charged current interactions. They will occur in the detectors or in the materials surrounding the detectors. To select the neutrino events, we applied the following selection criteria.

1. Select the beam-triggered events and reject the periodically triggered events. Also reject the events from dummy beam triggers which do not contain the real beam.

2. Apply time clustering cut (see section 3.3), select events which contains the time clusters. (Cut A)

3. Select the time clusters whose number of hits is greater than N_{min} . (Cut B) Where the parameter N_{min} is the minimum number of hits in the cluster.

We determine N_{min} in the following analysis.
There were many clusters which survived the Cut A. Most of those were clusters which contained only few hits, and they were also found in the periodic triggered events. An example of those event is shown in Fig. 5.1. We reject those events by adjusting the parameter N_{min} in Cut B.
In order to check what kind of events survived the Cut A, we checked the distribution of [Mean photo-electrons of the hits in the clusters] vs. [The number of hits in the clusters] (Fig. 5.2). In this figure, the mean photo-electrons are $\sim$30 p.e. for the clusters associated with many hits, which is close to the mean photo-electron of the hits from minimum ionizing particles (see section 4.2.5). In fact we clearly see particle tracks for those events (Fig. 5.3). On the other hand, for the clusters which have only few hits, the mean photo-electrons of the hits are much smaller than the mean photo-electrons of cosmic-ray hits. However the neutrino events should contain the hits of charged particles, and photo-electrons of the hits for those signals are usually comparable or bigger than the photo-electrons of cosmic-ray hits. Therefore we reject those small hits as background hits for this analysis. The source of these background clusters are considered as clusters with accidental noise hits or environmental radioactivity.

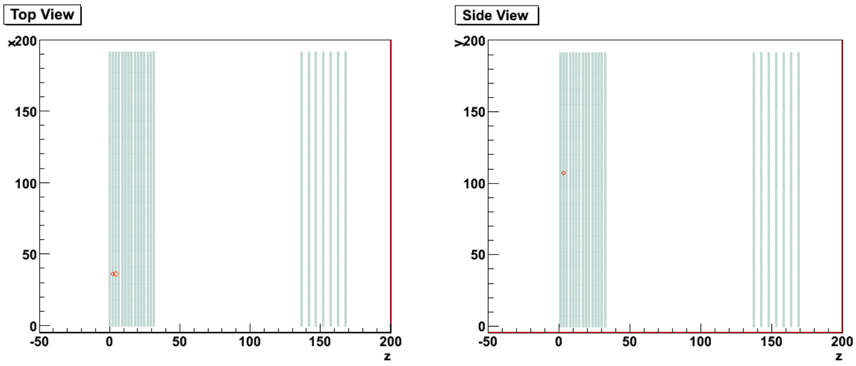

Figure 5.1: Typical event which contains only few hits in the cluster.

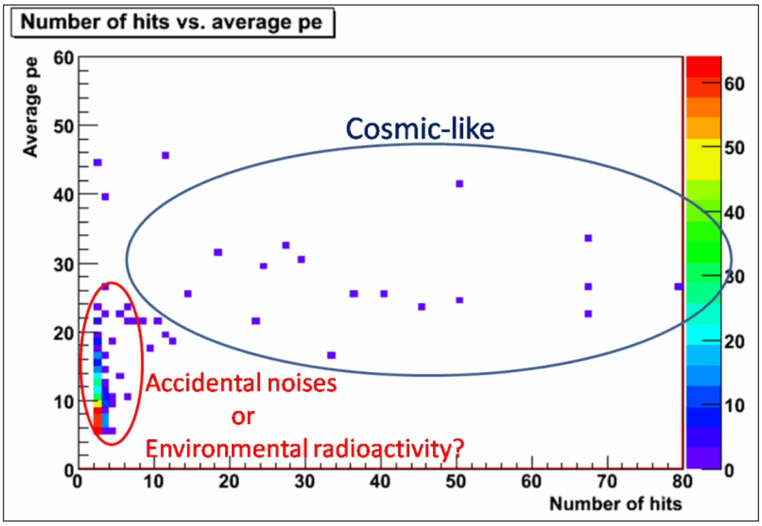

Figure 5.2: Mean photo-electron vs. number of hits in the cluster.

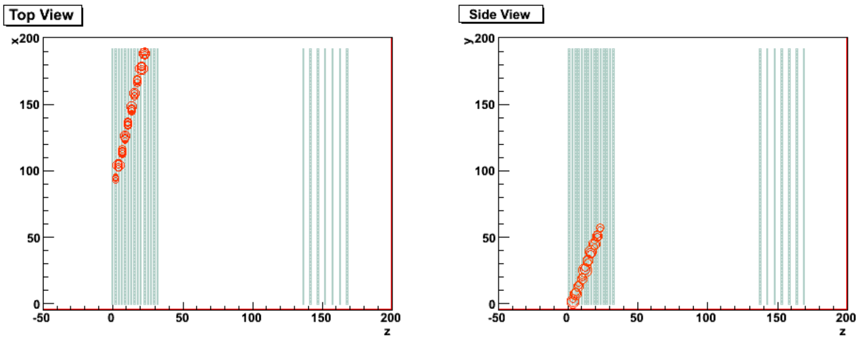

Figure 5.3: Typical event which contains >10 hits in the cluster.

In order to determine the parameter N_{min}, we checked the distribution of the number of hits for the clusters (Fig. 5.4). To reject most of the background hits we determined the parameter $N_{min} = 4$.

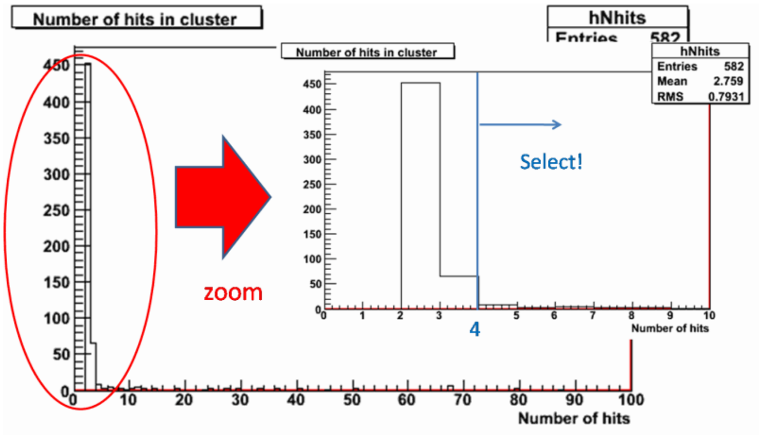

Figure 5.4: Number of hits in the cluster in the beam data.

We applied the selection cut for the data of the two beam runs. There were 8478 beam-triggered events (not including dummy beam triggered events), 382 clusters surviving Cut A, and 69 clusters survived Cut B. Figure 5.5 shows the timing distribution of the clusters which survived the cuts in the two runs. The timing of each clusters is defined as the mean timing of hits in those clusters. In this timing distribution, there is a peak around 3000 ns, which is the expected time of the first bunch calculated based on the delay of the electronics. The red broken lines shows the timing for six bunches, which is drawn according to the timing of first bunch and 581 ns separation between each bunch. There are 8 clusters found in the timing of

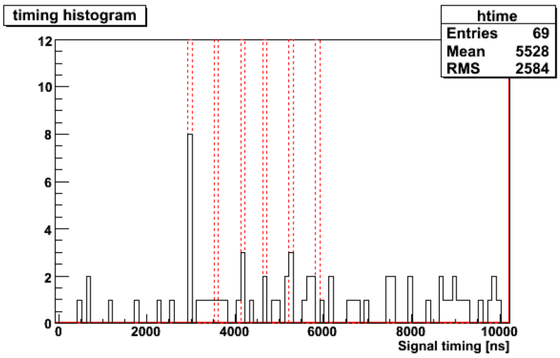

Figure 5.5: Timing histogram of beam triggered events. (1bin = 100 ns)

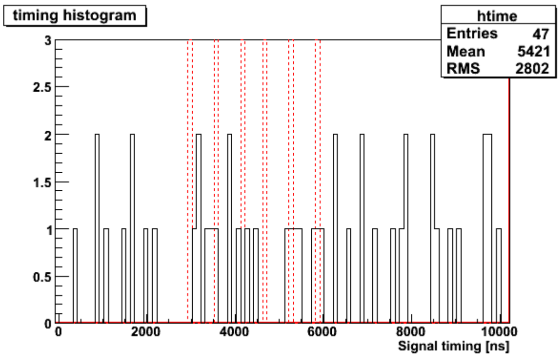

Figure 5.6: Timing histogram of periodically triggered events. (1bin=100 ns)

first bunch, and 17 clusters found in total in six bunches.
We also checked periodically triggered events to estimate the background. There were 12393 periodic triggered events, 483 clusters survived Cut A, and 47 clusters survived Cut B. From this result, we calculated the expected number of background clusters for each bins.

$$47\,\mathrm{clusters} \times \frac{8478\,\mathrm{beam\,triggered\,events}}{12393\,\mathrm{periodic\,triggered\,events}} \div 103\,\mathrm{bins} = 0.31\,\mathrm{clusters}/100\mathrm{ns} \quad (5.1)$$

This is much smaller than the clusters which we found in the first bunch timing for beam triggered event. For six bunches the expected number of background clusters is $0.31 \times 6 = 1.9$, which is also much smaller than observed number 17. We confirmed that our detector observed the neutrino events.
Figure 5.7 is an example of neutrino candidate event observed in the second run. Most of the events observed in the timing around the red lines contain horizontal going tracks. These tracks are explained as the tracks of muons produced in the neutrino interaction, and they are much different from the cosmic-ray tracks which are typically more vertical going. The events which occurred outside of the expected beam time do not look like the neutrino events, and they were similar to the background events shown in Fig. 5.3 and Fig. 5.1. Most of those events contained vertical tracks of cosmic-ray like.

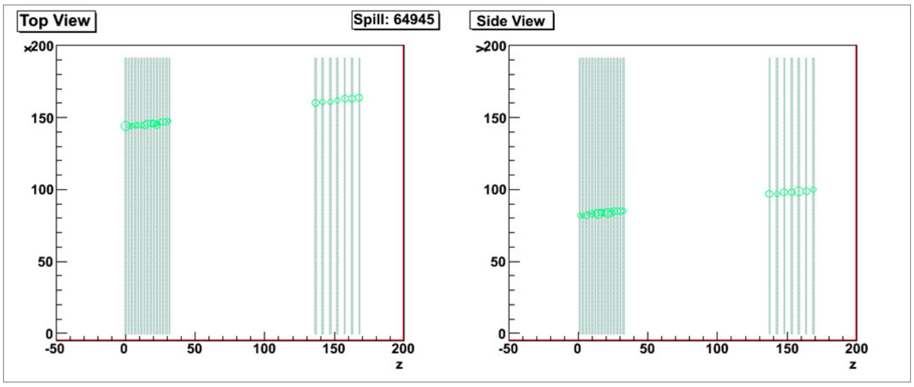

Figure 5.7: Example of neutrino candidate event.

To summarize, we successfully observed 17 neutrino candidate clusters where the expected number of background clusters is 2.3. We confirmed that the beam timing is consistent with the expected timing within ± 100ns.

Chapter 6

Summary

The FGD (Fine-Grained Detector) is a finely-segmented scintillator detector that form a part of T2K near detector. It is designed to to measure the neutrino beam flux and energy spectrum by detecting the tracks of charged particles from neutrino interaction.

We constructed the FGD at TRIUMF. The detector response to the various types of particles were tested in the beam test at TRIUMF M11 beam line together with the electronics test. The MPPCs are the photon detectors to detect the light from the scintillator bars. We tested their properties on the real detector, and confirmed that the properties are consistent with the test in Kyoto before shipment. We also tested the hit pre-selection algorithm in the beam test. The parameters for this selection are determined from the beam test data, and we successfully cut more than 99.9% of noise hits with the hit selection algorithm.

After the beam test, the FGDs were shipped to Tokai and reassembled there in June and July 2009. They were installed in the ND280 pit in October 2009. At this stage we tested the MPPCs, electronics modules and checked the performance of the detector.

The MPPCs were tested with fully installed electronics, and most of them worked fine except for $< 1\%$ of bad channels. Then we measured the break-down voltage of the MPPCs to apply the correct bias voltages for all the channels.

The Cosmic Trigger Module (CTM) is the module to provide the cosmic-ray trigger. The module was tested and worked fine, and the events triggered by the CTM is studied. The method for timing synchronization, which use the timing marker signal from CTM, was tested and worked correctly. The timing resolution of the detector was 4.9 ns.

We checked the performance of the scintillator bars. The light yield for the MIPs is measured in the function of path length. Also we checked the hit efficiency for scintillator planes, and confirmed that they are more than 99%, as required.

Finally we launched into first neutrino beam data taking, and searched for the neutrino candidate events. As a result, we successfully observed 17 neutrino candidate events around the expected beam timing.

Acknowledgement

I would like to thank many people for helping me to realize this thesis.

First of all, I would like to express my gratitude to Prof. Tsuyoshi Nakaya, for always leading me to the right way. His advice was always critical and thoughtful.
I also want to express my thanks to Prof. Masashi Yokoyama and Prof. Atsuko Ichikawa, who gave me a lot of advice for my analysis.

In the year of 2009, I spent a lot of time working with people from Canadian group. I am really glad to have been able to work with them. I would like to thank Dr. Scott Oser, Dr. Hiro Tanaka, Dr. Thomas Lindner, Dr. Fabrice Retiere, and all other people who worked with me.

I also would like to express lots of thanks to the members of High Energy Physics Group at Kyoto. My two years of master course was a lot of fun.
Finally, I would like to send my best thanks to my family.

Bibliography

[1] Ziro Maki, Masami Nakagawa, and Shoichi Sakata. Remarks on the unified model of elementary particles. Prog. Theor. Phys., Vol. 28, pp. 870.880, 1962.

[2] Y. Ashie, et al. A Measurement of Atmospheric Neutrino Oscillation Parameters by Super-Kamiokande I. Phys. Rev., Vol. D71, p. 112005, 2005.

[3] M. H. Ahn, et al. Measurement of Neutrino Oscillation by the K2K Experiment. Phys. Rev., Vol. D74, p. 072003, 2006.

[4] D. G. Michael, et al. Observation of muon neutrino disappearance with the MINOS detectors and the NuMI neutrino beam. Phys. Rev. Lett., Vol. 97, p. 191801, 2006.

[5] B. Aharmim, et al. Electron energy spectra, fluxes, and day-night asymmetries of B-8 solar neutrinos from the 391-day salt phase SNO data set. Phys. Rev., Vol. C72, p. 055502, 2005.

[6] J. Hosaka, et al. Solar neutrino measurements in Super-Kamiokande-I. Phys. Rev., Vol. D73, p. 112001, 2006.

[7] S. Abe, et al. Precision Measurement of Neutrino Oscillation Parameters with KamLAND. Phys. Rev. Lett., Vol. 100, p. 221803, 2008.

[8] M. Apollonio et al. (CHOOZ Collaboration). Search for neutrino oscillations on a long base-line at the chooz nuclear power station. Eur. Phys. J., Vol. C27, p. 331, 2003.

[9] N. Nagai “T2K 実験において用いられる半導体光検出器 MPPC の大量測定”

[10] K. Hiraide “J-PARC ニュートリノ振動実験のための off-axis 前置検出器の基本設計および APD 読み出し系の開発”